Technische Universiteit Delft Netherlands

COMBINED AB-INITIO AND EXPERIMENTAL STUDY OF HYDROGEN SORPTION IN DUAL-PHASE STEELS

Saurabh Sagar

August 2020

COMBINED AB-INITIO AND EXPERIMENTAL STUDY OF HYDROGEN SORPTION IN DUAL-PHASE STEELS

A thesis submitted to the Delft University of Technology in partial fulfillment
of the requirements for the degree of

Master of Science in Materials Science and Engineering

by

Saurabh Sagar

August 2020

Saurabh Sagar: *Combined Ab-initio and Experimental Study of Hydrogen Sorption in Dual-Phase Steels* (2020)

The work in this thesis was made in the:

Department of Materials Science and Engineering
Faculty of Mechanical, Maritime and Materials Engineering
Delft University of Technology

Thesis Committee: Dr. Vera Popvich, TU Delft
Dr. Poulumi Dey, TU Delft
Dr. Marcel Sluiter, TU Delft
Pascal Kömmelt, Tata Steel Europe

ABSTRACT

The formability of Advanced High Strength Steels is critical for their usability in automotive applications. It has been observed that the presence of hydrogen, even in concentrations of the order of 1 ppm, leads to a considerable drop in formability. Hydrogen atoms may get absorbed during steel-making and are known to get trapped at various sites in the lattice. When sufficient activation energy is made available, hydrogen atoms that are weakly trapped can diffuse towards critical regions in the microstructure, such as crack tips and voids, where one or more embrittlement mechanisms might be activated. On the other hand, a strongly trapped hydrogen atom remains immobile and plays no part in the embrittlement process. Precipitates of transition metals are known to be strong traps for hydrogen. It is speculated that by promoting the formation of strong traps in the microstructure, the amount of freely diffusible hydrogen can be limited, which would lead to an improvement in mechanical performance.

In this work, a combined ab-initio - experimental approach was used to study the absorption of hydrogen in dual-phase steel. Density Functional Theory (DFT) calculations were employed to study and compare the trapping of hydrogen by carbide and nitride of titanium and vanadium. A carbon or nitrogen vacancy in the bulk of the precipitate was found to be the most efficient trap site. When coupled with the vacancy formation energy, trapping was found to be more efficient in off-stoichiometric vanadium carbide and nitride than that in titanium carbide and nitride. To validate the theoretical findings, cyclic voltammetry experiments were conducted on two grades of DP800 steel with different concentrations of vanadium and titanium. The amount of diffusible hydrogen in the vanadium grade was found to be approximately 25 % higher than that in the titanium grade. This was in contradiction to the theoretical results. Characterisation of the specimen post testing revealed that an oxide film had formed on the sample surface and while the film on vanadium grade was uniform and dense, that on titanium grade was sparse and irregular. It was evident that the oxide layer contributed to trapping of hydrogen, however the amount of hydrogen trapped by the oxide could not be specified. Overall, designing steels resistant to hydrogen embrittlement by promoting the formation of precipitates of a particular element is theoretically attainable, however, it was not possible to obtain experimental validation with the method employed.

ACKNOWLEDGEMENTS

I would like to thank Dr. Vera Popovich and Dr. Poulumi Dey for giving me the opportunity to work on this thesis and the guidance and support that I received throughout my work. I would also like to thank Pascal Kömmelt for sharing his expertise and enthusiasm on the subject. I extend my gratitude towards Dr. Yaiza Gonzalez Garcia for the insightful discussions on electrochemical aspects of this work. I am also grateful to Agnieszka Koojiman for her invaluable guidance and support in conducting the electrochemical experiments. I would also like to thank Ruud Hendrikx for his support on the XRD experiments, and Sander van Asperen and Kees Kwakernaak for their guidance on microscopy techniques. Last but not the least, I am grateful to my parents for their love, support and patience.

CONTENTS

LIST OF FIGURES

LIST OF TABLES

ACRONYMS

HE:	hydrogen embrittlement
DFT:	density functional theory
AHSS:	advanced high strength steels
HID:	hydrogen induced decohesion
HELP:	hydrogen enhanced localised plasticity
HESIV:	hydrogen enhanced strain induced vacancy
HIPT:	hydrogen induced phase transformation
AIDE:	adsorption induced decohesion
CV:	cyclic voltammetry
SEM:	scanning electron microscope/microscopy
FTIR:	fourier transform infra-red

1 MOTIVATION

For a long time it had been well known to wire-drawers and other manufacturers, who removed rust from iron or steel by cleaning it with sulphuric acid, that after this process the metal becomes more brittle. In 1875, Johnson documented the findings from a series of experiments aimed at examining this effect [13]. Upon immersing an iron wire in sulphuric acid, the wire was found to have become more brittle. When the fracture surface was wetted, copious bubbles of gas were given off from the whole surface of the fracture. These bubbles of gas were collected in a bell jar and were found to burn with the characteristic flame of hydrogen. The frothing and reduction in toughness was only temporary, as when the wire was left at ambient temperature for 3 days, or at a higher temperature of 200 °C for half a day, the original toughness was restored and no bubbles were observed on moistening the fracture surface. Furthermore, the hydrogen had to be nascent, not molecular, since leaving it in hydrogen gas did nothing to the mechanical properties. In the same work, the action of acid on steels as compared to iron was found to be more rapid and more prominent. On hardened and tempered steel, the decrease in toughness was greater and more rapid than steel in soft state. It was also observed that the higher the carbon content, more pronounced and more irreversible was the deterioration.

This comprehensive series of experiments laid the foundation for decades of research on the influence of hydrogen on iron and steel. The intricate phenomena of deterioration of mechanical properties of materials in the presence of hydrogen has since been termed as *Hydrogen Embrittlement* (HE). Problems connected to hydrogen in materials manifest in numerous ways, e.g. stress corrosion cracking, hydrogen-induced cracking and surface blistering as well as reduction in ductility. It has been well documented that hydrogen, even in small quantities of the order of 1 ppm, can lessen the mechanical properties. This is of particular concern in steelmaking, as there is a possibility of absorption of hydrogen during processes like acid pickling, electroplating and annealing, or even during the service life of the material.

Presently, advanced high strength steels are widely used for making structural components for automobiles [14]. Such steel grades possess high strength *and* enhanced ductility and are characterised by multiphase microstructures and carefully selected chemical compositions. Formability is one of the most critical properties of AHSS for their suitability to automotive applications. Fan and Pielet studied the local formability of hot dip galvanised dual phase steel by performing 90 degree V bend tests [1]. Hydrogen was introduced into the steel at the final stage of processing while the steel was coated with zinc. As shown in Figure 1.1, the failed samples had large surface cracks, indicative of a potential failure when the same steel is stamped to make automotive parts. The ductility of steel around bend zones and sheared edges is commonly referred to as edge ductility. To investigate whether hydrogen has any influence on edge ductility, the same material was subjected to a hydrogen removal process. The zinc coating was removed chemically and the sample was left to sit in ambient temperature for 24 hours to allow the hydrogen to diffuse out and the bendability was subsequently measured. Bendability is generally measured as the minimum ratio of the punch radius (r) to the strip thickness (t) that the steel can tolerate without the appearance of surface defects during bending to an angle of 90 ° in three-point bending [15]. The observed r/t values and me-

chanical properties are listed in Table 1.1. It was seen that as the diffusible hydrogen content was reduced after coating removal, the bendability improved from 3.9 r/t to 1.6 r/t.

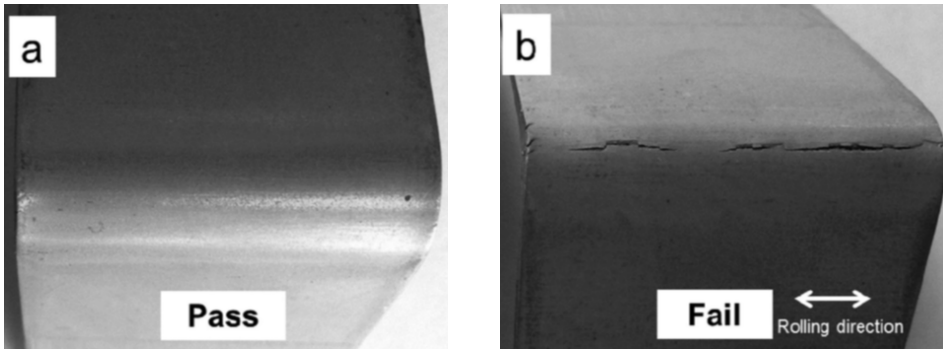

Figure 1.1: Examples of (a) passed and (b) failed bend coupouns of DP980 steel [1]

Condition	Yield Strength, MPa	Tensile Strength, MPa	r/t	diff H, ppm
As produced	707	1070	3.9	0.42
Coating removed			1.6	0.04

Table 1.1: Properties of DP980 steel before and after hydrogen removal [1].

Similar tests on other mechanical properties such as tensile strength and fracture toughness also indicate that controlling the amount of diffusible hydrogen can help in improving the material's resistivity to HE. Resistance to HE in AHSS is crucial to their application, not only in regard to improving their performance, but also in making them safe and reliable for use in consumer goods.

Beyond its significance to the steel industry, the vision of a hydrogen economy is gaining worldwide support. Hydrogen, as a low carbon fuel alternative, has the advantages of being light, storable and energy dense and produces no direct emissions of pollutants or greenhouse gases. This has led to its use in the industry sector, such as oil refining, ammonia production and methane production, as well as in the transport sector. Consequently, the demand for hydrogen has increased threefold since 1975, while policy support for hydrogen based services is also gaining prominence [2]. Figure 1.2 shows the major sectors that are part of the hydrogen economy and the policy support provided by governments through incentives and targets. There is already significant support for hydrogen vehicles, while its use in power generation and industry is expected to grow. Development of auxiliary processes such as hydrogen storage, transport and transfer are significant for the hydrogen economy. Such systems are also subjected to the same concerns with regard to embrittlement as the automotive steel industry. As an example, the possibility of using pipeline steels for transporting hydrogen is practical only when the criteria for material failure under the influence of hydrogen have been established and a factor of safety can be defined. Therefore, research in the field of hydrogen embrittlement can be helpful in supporting the vision of a hydrogen economy.

While the manifestations of hydrogen embrittlement have been well documented, its exact nature is still an open area for research. The experimental difficulty in detecting hydrogen directly is a hindrance to obtaining detailed information on the phenomenon. Hydrogen, being the lightest element on the periodic table, is highly

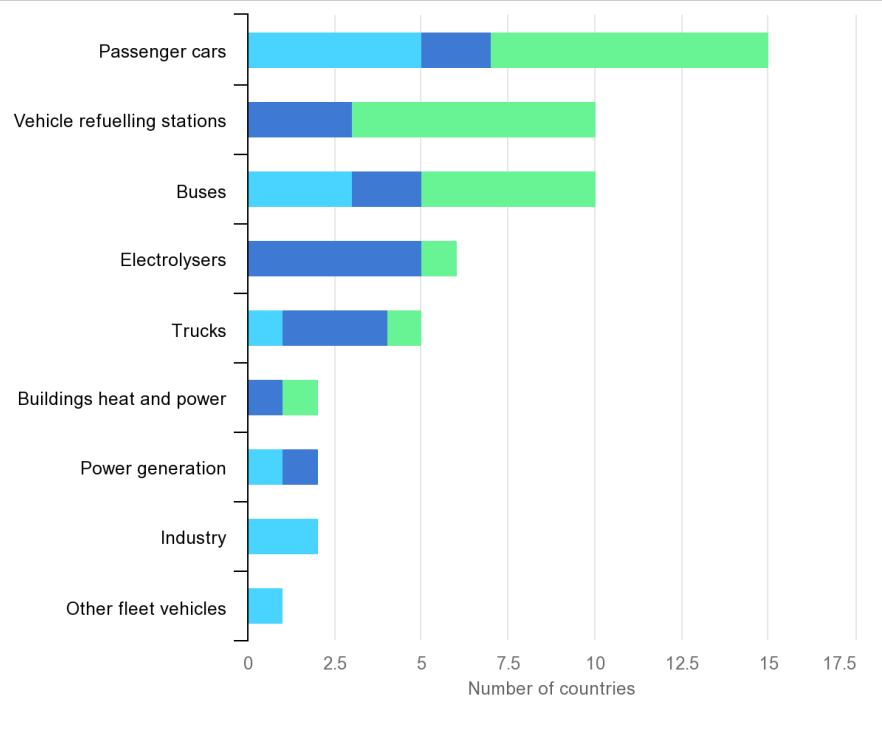

Figure 1.2: Policy support for hydrogen deployment in terms of targets and incentives, 2018 [2]

mobile and insensitive to external excitation. Coupled with normally very low concentrations of hydrogen, information on its states in materials is limited and most notions about the function of hydrogen have remained speculative. Moreover, the interaction of hydrogen with microstructural features such as dislocations and second phase particles can be quite complicated, leading to failure via one or more mechanisms. Thus there is a need for linking a material's properties in the presence of hydrogen with its microstructure.

1.1 OUTLINE OF REPORT

The report begins with a literature review of the various mechanisms of hydrogen embrittlement and the interaction of hydrogen with microstructural features. Following the synopsis, the research objectives and approach to the problem are listed. Chapter 3 is dedicated to materials and methods, and presents the materials that were selected for this study as well as their characterisation, along with details of the methods employed. Subsequently, results and discussion are presented in Chapter 4. In Chapter 5, some conclusions are drawn up and finally, recommendations for furthering the present research are presented in Chapter 6.

2 STATE-OF-THE-ART ON HYDROGEN EMBRITTLEMENT IN STEELS

HE is generally marked by the ductile-brittle transition of metals in the presence of hydrogen. The following section details the mechanisms through which this may occur. While it has been difficult for researchers to experimentally observe such phenomena, simulations have been utilised to obtain support for the underlying theory behind these mechanisms. In Section 2.2, current understanding of interaction of hydrogen with the microstructure, beginning with the absorption of hydrogen on the metal surface is presented.

2.1 MECHANISMS OF HYDROGEN EMBRITTLEMENT

2.1.1 Hydrogen induced/enhanced decohesion (HID)

The Hydrogen-induced decohesion theory hypothesizes that there is a reduction in bonding energy between atoms due to the presence of hydrogen, which consequently increases the risk of decohesion. According to this model, HE occurs within the crack tip fracture process zone, when the tensile stresses exceed the local atomic cohesive strength, which is reduced in the presence of hydrogen. The HID mechanism was initially proposed by Gerberich et al. in the 1970s to explain the observed decrease in crack-tip-opening angle with increasing hydrogen content [3]. The HID mechanism is supported by the fact that hydrogen tends to diffuse to areas of high stress, similar to that found ahead of a crack tip. Gerberich's experiments remain the predominant experimental proof for HID (Figure 2.1 and 2.2)

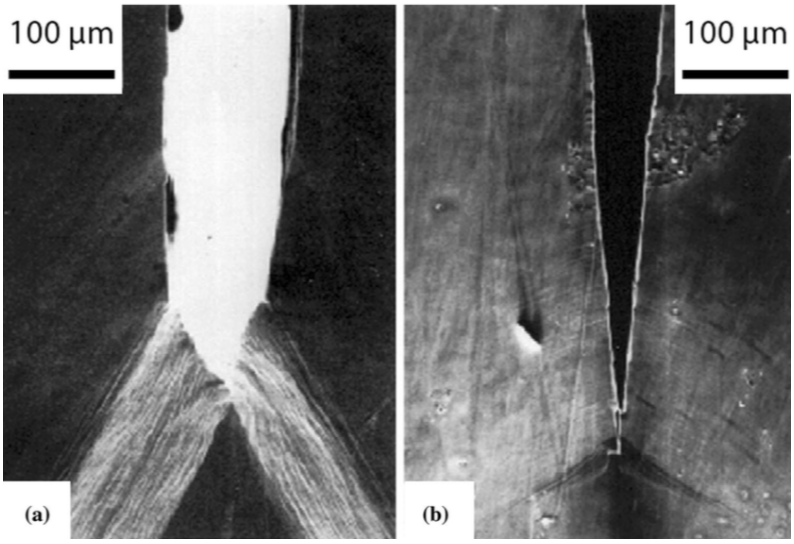

Figure 2.1: Crack-tip-opening angles of a Fe–Si (3 wt%) single crystal after straining in a) vacuum and b) hydrogen [3]

The reduction in cohesive strength has successfully been demonstrated through simulations. Using Cohesive Zone Modelling (CZM), Katzarov and Paxton found that the cohesive strength across two (111) planes in α-Fe decreased from 30 to 22

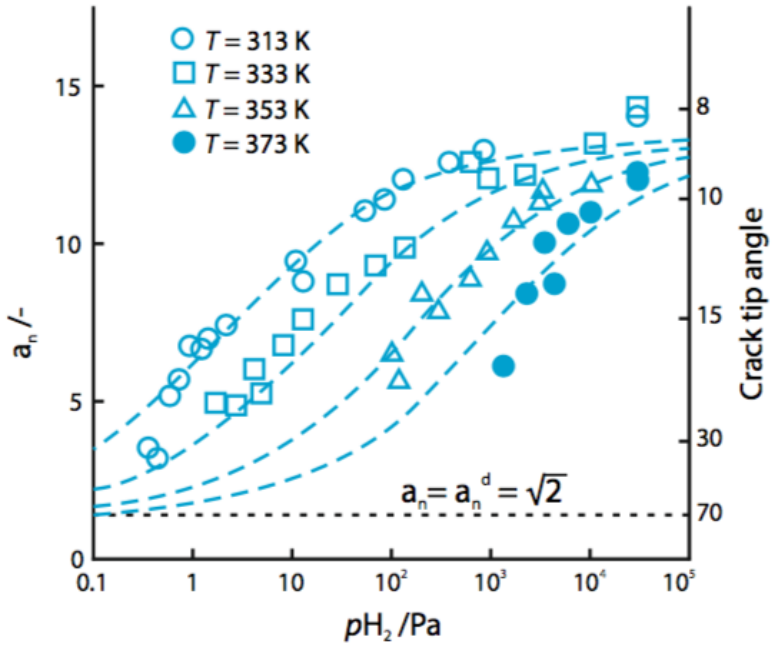

Figure 2.2: Crack-tip-opening angle as a function of in situ hydrogen pressure for a Fe–Si (3 wt%) single crystal over a range of temperatures. The horizontal dashed line indicates crack growth solely by crack tip slip [3]

GPa as a result of dissolved hydrogen [16]. Similarly, Wang et al. predicted a 37% drop in the cohesive energy using an empirical embedded atom model potential (EAM), across a wide range of Fe grain boundaries that span the complete range of misorientation angles [17]. It should be noted that HID remains unproven by direct experimental methods. At the cutting edge of research aimed at legitimising this mechanism is the desire to demonstrate the effect of the dissolved atomic hydrogen on (a) lowering the interatomic force–displacement relationship in metals and the resultant effects on surface energies, (b) the material properties that induce the observed changes in the mechanical behaviour.

2.1.2 Hydrogen enhanced localised plasticity (HELP)

Beachem in the 1970s was one of the first to have hypothesised that under specific conditions (temperature, hydrogen concentration etc.), hydrogen dissolved in the lattice enhances ductility by reducing the threshold stress to unlock dislocations, i.e. in the presence of hydrogen dislocations can move at a reduced stress [18]. This causes severe local plastic deformation, leading to fracture which is macroscopically brittle in appearance and behaviour. Increased dislocation mobility with hydrogen in austentic stainless steels was observed by Ferreira et al. [4] by using in situ hydrogen charging within an environmental TEM. The observed result was an increase in the dislocation mobility leading to an increased density of dislocation pile-ups at interfaces such as second phase particles or grain boundaries as shown in Figure 2.3. Although the authors cite that free hydrogen in solid solution reduces the critical stress for dislocation movement by shielding the elastic field around dislocations, more recent studies [12] have shown that HELP is due to reduction in the stacking fault energy; reducing susceptibility to cross-slip by increasing the equilibrium distance between partial dislocations. However, softening due to the presence of hydrogen does not independently lead to a macroscopic brittle response and softening must be combined with other degradation process such as HID for the material to embrittle.

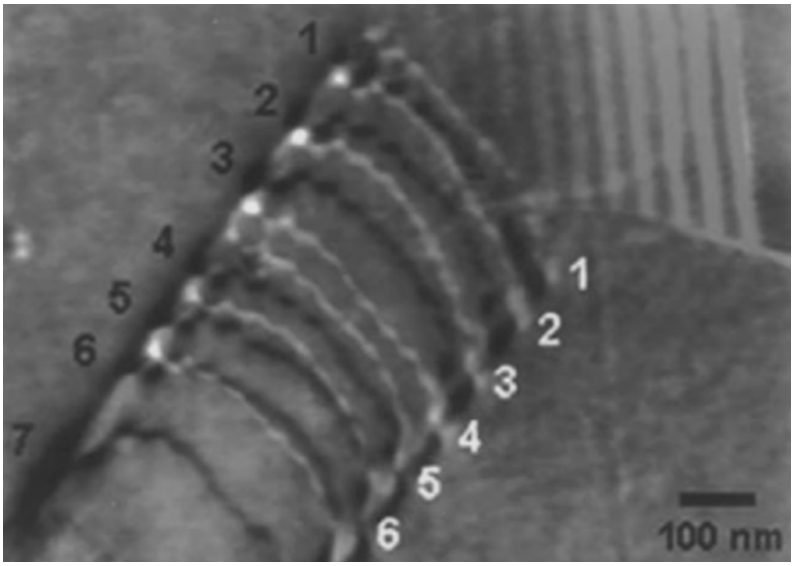

Figure 2.3: Superimposition of two TEM images of a single dislocation pile-up upon a grain boundary under constant stress; one within a vacuum (black), the other under 95 Torr of Hydrogen gas (white) in 310 S stainless steel [4]

The increase in velocity of dislocations in the presence of hydrogen has been supported by simulations [16]. In this paper, the authors use published first-principles (DFT) data on hydrogen dislocation interactions to build a kinetic Monte Carlo model for the calculation of dislocation velocity in α-Fe as a function of stress, temperature, and bulk hydrogen concentration. The most relevant findings were that the effect of hydrogen on increasing dislocation velocity is strongest at low temperature and low hydrogen concentration and the range of hydrogen concentration within which dislocation velocity increases most significantly widens with increasing temperature.

2.1.3 Hydrogen induced phase transformation (HIPT)

In FCC alloys such as austenitic stainless steels subjected to hydrogen charging, a large supersaturation of hydrogen can create significant structural changes in the surface layer of the specimens. This phenomenon is known as hydrogen-induced phase transformation. Two types of phase transformations have been observed: (a) hydride formation and (b) hydrogen-induced martensitic transformation.

Hydride forming materials such as zirconium, titanium and other transition metals experience cracking when the hydrogen content exceeds the solubility limit [19]. The hydride precipitates are quite brittle, resulting in a low energy fracture path through these precipitates. Hydrogen-induced martensitic transformations consist of the FCC austenite phase transforming into either the HCP phase (ϵ martensite) or the BCT phase (α martensite). The martensitic phase exhibits higher diffusivity for hydrogen than the austenite phase, thus providing fast pathways for hydrogen to diffuse to areas of high stress concentration [20].

2.1.4 Hydrogen enhanced strain induced vacancy formation (HESIV)

The hydrogen-enhanced strain-induced vacancy (HESIV) formation theory suggests that the density and clustering of vacancies is enhanced in the presence of hydrogen. Vacancies can coalesce to form microvoids, which in turn may combine to form larger voids leading to a decrease in ductile crack growth resistance. This phenomenon can be observed during tensile testing and fracture toughness testing of hydrogen-charged samples [21]. In this work on INCONEL and iron alloys, it

was found that hydrogen-charged samples had a higher void density after the same fatigue cycles as the uncharged samples. A considerable amount of experimental data further support the effect of hydrogen on vacancy formation [12].

2.1.5 Adsorption induced decohesion (AIDE)

It was first suggested by Lynch that hydrogen assisted cracking may also occur via direct adsorption of hydrogen at the crack tip [22]. There is evidence of the embrittlement of metals (aluminium alloys, nickel, titanium alloys and magnesium) in aqueous or hydrogen environments, observed at crack velocities which are too high to allow the hydrogen to diffuse ahead of cracks. The author's conclusion was that such a mechanism occurs because adsorption facilitates the emission of dislocations from crack tips and thereby promotes the coalescence of cracks with voids ahead of the crack, leading to increased crack growth rates. There is, however, no direct evidence for the increased crack propagation due to dislocation emission from crack tips.

In Table 2.1, a short summary of the important HE mechanisms has been presented. The mechanisms discussed above were proposed to explain specific instances of hydrogen embrittlement and it is expected that a combination of any of these mechanisms may occur simultaneously. However, for embrittlement to occur through any of these mechanisms, the diffusion of hydrogen to crack tips and grain boundaries or vacancies is vital. The amount of diffusible hydrogen strongly depends on the microstructure of the material. Indeed, it has been shown that modifying the microstructure by introducing 'hydrogen traps' can reduce the amount of diffusible hydrogen and therefore contribute to mitigating its harmful effects [23].

2.2 HYDROGEN UPTAKE AND INTERACTION WITH MICROSTRUCTURAL FEATURES

To overcome hydrogen embrittlement, it is firstly important to understand how is hydrogen absorbed in the material and what is the nature of its interactions with the microstructure. It must be noted that direct evidence of hydrogen is limited. However, atomistic simulations have filled in some of the gaps in our understanding of hydrogen interactions with the microstructure. Pertinent findings are reviewed in this section.

2.2.1 Hydrogen absorption

Hydrogen may be directly absorbed from the gaseous state at several stages during steelmaking, most commonly during the final annealing step. The solubility of diatomic gases in a melt is generally governed by Sievert's law, which states that at a given temperature, solubility is directly proportional to the square root of partial pressure. Based on empirical data, Hirth expressed solid solubility (θ, in atomic ratio) in Hydrogen gas of pressure P (0.1 MPa) in the form

$$\theta = 0.00185\, P\, exp\,(\frac{-3440}{T}) \tag{2.1}$$

with T in Kelvin [24]. Hydrogen absorption can also occur in an aqueous environment, as a consequence of electrochemical processes, e.g. during pickling or corrosion of steels. Much higher hydrogen concentrations and hence more severe damage is caused in this manner, as compared to the absorption of gaseous hydrogen. The adsorption of hydrogen from an aqueous solution takes place through a

Mechanism	Postulate	Evidence	Remarks
HID	Reduction in atomic bond strength in the presence of H, leading to decohesion.	Reduction in crack tip opening angle with increasing H partial pressure, indicating an increase in brittleness.	The effect of the dissolved atomic Hydrogen on lowering the interatomic force–displacement relationship in metals needs to be explored further.
HELP	Increased mobility of dislocations leading to localised plastic failure	Increased density of dislocation pile-ups at interfaces in austenitic stainless steels.	Additional mechanisms such as HID are necessary for fracture to initiate.
HIPT	Increase in density and clustering of vacancies in the presence of Hydrogen.	Increased void density in H charged iron alloys such as INCONEL after a few fatigue cycles.	HESIV by itself is not sufficient to explain HE.
HESIV	Brittle hydride or martensitic phases under large supersaturation	Hydrogen Induced martensitic transformation in Fe-Ni alloys	High supersaturation of H is necessary. The role of strain-induced martensite in hydrogen embrittlement needs further clarification
AIDE	Direct adsorption of H at surface cracks/voids leading to fast crack growth.	No direct evidence, although embrittlement has been observed at crack velocities which are too high to allow the hydrogen to diffuse ahead of cracks.	Direct evidence is lacking

Table 2.1: Summary of HE mechanisms, adapted from [12]

sequence of electrochemical reactions. The electrochemical reduction process proceeds by the Volmer reaction described by:

$$H^+ + e^- \Longleftrightarrow H_{ads} \tag{2.2}$$

or,

$$H_2O + e^- \Longleftrightarrow H_{ads} + OH^- \tag{2.3}$$

where reaction 2.2 is the predominant reduction mechanism in an acidic environment. The adsorbed hydrogen atoms may be absorbed into the metal or may recombine chemically to form molecular hydrogen, which then dissolves in the solution according to the Tafel reaction.

$$2H_{ads} \Longleftrightarrow H_2(aq) \tag{2.4}$$

The extent of hydrogen absorption is a function of the relative rates of generation and recombination with respect to the diffusion flux of hydrogen into the metal. Generally, most of the hydrogen atoms recombine to form molecular hydrogen, but this may be influenced by the presence of absorption promoters such as arsenic or hydrogen sulphide in the solution.

Entry of hydrogen into the bulk of a transition metal is commonly considered to occur via chemisorption of atomic hydrogen on the surface and involves the following steps:

- Transport of the H_2 molecule to the surface.
- Molecular adsorption (physisorption).
- Dissociation of H_2 and formation of a chemisorption bond between atomic hydrogen and a surface site consisting of a certain number of substrate atoms. This dissociative adsorption may or may not be an activated process.
- Transfer of surface-adsorbed hydrogen to hydrogen dissolved beneath the surface.
- Diffusion into the bulk phase.
- Possibly hydride formation near the surface when the hydrogen concentration reaches a critical value.

The adsorption steps can be explained with the help of a Lennard Jones diagram. In Figure 2.4, the potential energies of a hydrogen molecule and two separated hydrogen atoms are plotted as a function of distance from the metal surface. The energy of H_2 molecule far from the surface is set as zero while that of the H atoms is higher, the difference between the two being the energy of dissociation of a H_2 molecule. Owing to the electrostatic fields around the metal surface, the two species have potential minima at some distances from the surface which correspond to molecular and atomic adsorption states. The potential energy curves of the two species cross each other at some distance from the surface and the crossover point can be considered as a point of dissociation of a molecule, as the potential energy of H atom is lower beyond this point. After dissociation, the two individual atoms chemisorb separately. Beyond the metal surface, there exist several potential states as a consequence of the unique coordination states of some atoms in the imperfect lattice. This diagram is a simple representation of this complex process and in reality, depends on many factors such as defects, impurities, surface coverage, and surface reconstruction as well as the electronic state of the metal surface.

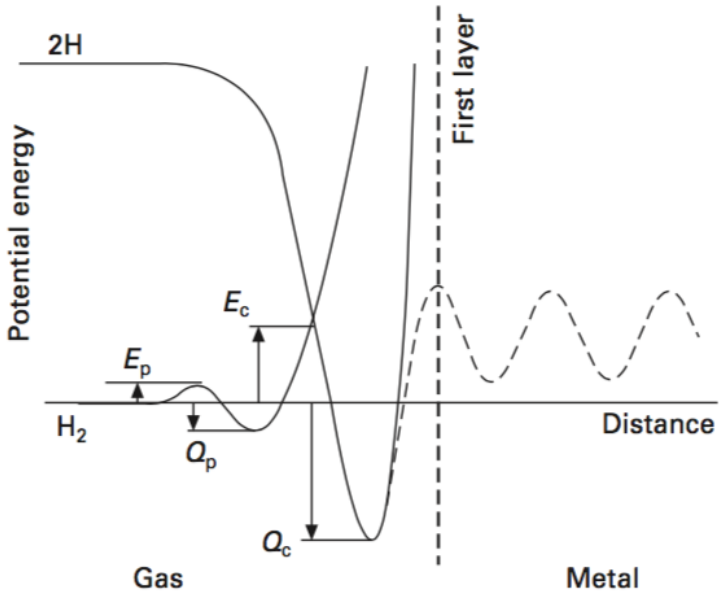

Figure 2.4: Potential energies of two free atoms and a molecule near the gas-solid interface [5]. E_p and E_c are the activation energies for physical adsorption of the molecule and chemical adsorption of two dissociated atoms, while Q_p and Q_c are the heats of adsorption of molecules and atoms, respectively.

The sub-surface lattice hydrogen concentration is a repercussion of the severity of the environment, and is the key parameter determining concentration-driven diffusion in the metal. The classical picture of hydrogen diffusion is that it occurs via hopping of hydrogen atoms between interstitial lattice sites. The preferred interstitial sites in BCC metals tend to be tetrahedral sites at ambient temperatures, as the radius of the tetrahedral site is about twice that of the octahedral site and can more easily accommodate the hydrogen atom at low temperatures. For FCC metals or alloys such as austenitic stainless steels the preferred sites are octahedral, while for HCP metals and alloys the preferred sites are tetrahedral at ambient temperatures. The distance between nearest neighbour interstitial sites in a BCC lattice is typically 0.11 nm (tetrahedral sites) while for the FCC lattice a value of 0.18 nm is more typical. Consequently, the activation energy for hydrogen diffusion is smaller in a BCC lattice as compared to the FCC lattice. The small size of hydrogen atom also facilitates quantum tunneling across interstitial sites, thus providing a separate mechanism for diffusion.

Apart from the normal interstitial lattice sites, hydrogen atoms can get trapped at certain microstructural sites such as grain boundaries, dislocations, vacancies, precipitates and other defects. Figure 2.5 is a schematic of the various *trap sites* that can be found in a lattice. The potential energy of hydrogen atom close to lattice defects in metals is mostly lower than that in regular interstitial lattice sites due to elastic and electronic interactions, causing the hydrogen atom to sit in the site for longer than in the lattice site.

Traps in the microstructure are characterised by the activation energy for (de-) trapping and the binding energy of the hydrogen atom within the trap. It follows that hydrogen can be bound more strongly at certain trap sites than at others. For very deep potential wells, there is effectively zero probability of the hydrogen atom jumping out of the trap site and these sites are referred to as irreversible trap sites. Accordingly, an irreversible trap is desirable, as it limits the amount of diffusible hy-

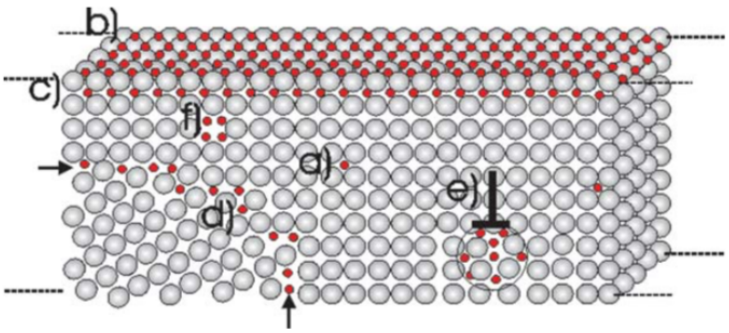

Figure 2.5: Schematic representation of various locations for accumulation of hydrogen. Along with the conventional solubility in lattice sites (a), trap sites on surface (b) and subsurface (c), grain boundaries (d), dislocations (e) and vacancies (f) [6]

drogen, unlike reversible traps, which release the absorbed hydrogen at sufficiently high temperatures. The distinction between a reversible and irreversible trap is not exact, however, as the activation energy of de-trapping will be a function of temperature. Binding energies of different traps have been compared through Thermal Desorption Spectroscopy and atomistic calculations, and although the results are sensitive to the imposed conditions such as temperature, traps can, in general, be ranked in the following order of increasing trapping strength [25]:

- Solute atoms
- Free surfaces and subsurface layers
- Vacancies and vacancy clusters
- Dislocation cores and strain fields
- Grain boundaries including prior-austenite grain boundaries in martensitic steels
- Precipitate/matrix interfaces and strain fields around precipitates
- Inclusion/matrix interfaces
- Voids and internal cracks

Voids formed at interfaces, such as MnS inclusions, can also be classified as traps but with the distinction that these tend to be dynamic traps as they increase their capacity (near-surface blistering or internal void growth) in response to progressive hydrogen uptake and increased hydrogen gas pressure in the void. Such trapping at voids is an exception insofar as the void represents a dynamic sink for molecular hydrogen rather than atomic hydrogen.

Various lattice defects are produced in materials during thermal and mechanical processing, and the defects interact with hydrogen in their specific ways. The interactions are crucial for hydrogen embrittlement due to variations of hydrogen concentration around defects as well as the variation in densities and structures of defects. Observed hydrogen effects comprise contributions of various types of defects, but the separation of individual contribution is not straightforward.

2.2.2 Trapping by precipitates

Fine carbides or nitrides are widely utilized for grain refinement and precipitation hardening of steels. Interactions of hydrogen with such precipitates are particularly important for hydrogen embrittlement of high strength steels [9, 26]. Precipitates

are generally strong (irreversible) traps for hydrogen which can help in limitng the amount of diffusible hydrogen in the microstructure.

Takahashi et al. obtained direct atomic scale observation of deuterium atoms trapped at nano sized TiC precipitates using Atom Probe Tomography [7]. The elemental maps of hydrogen (deuterium) charged and uncharged samples are shown in Figure 2.6. Deuterium atoms were observed homogeneously along the broad surface of TiC platelets. The absence of deuterium in the matrix slightly far from the precipitates suggested that the trapping does not occur in the strain fields around the precipitate, but rather within the precipitate or at the interface between precipitate and matrix.

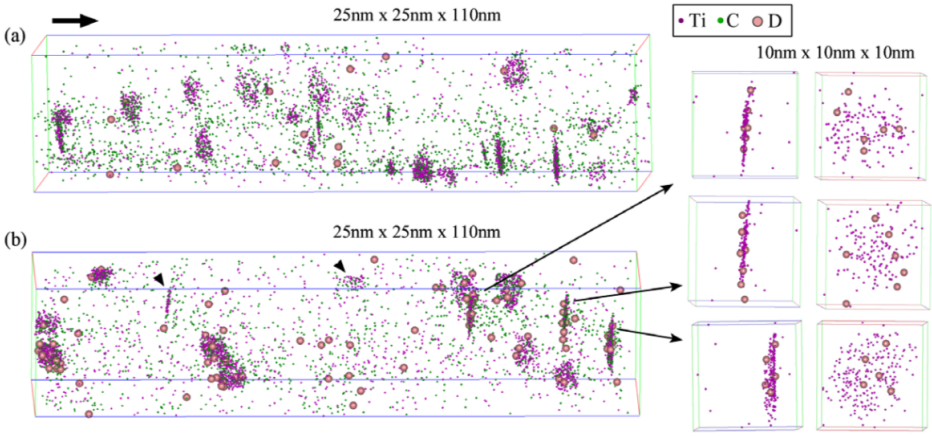

Figure 2.6: 3D elemental maps of (a) uncharged and (b) charged specimens as obtained by APT [7].

That the trapping in precipitates is *strong* was apparent in the work of Malard et al., who evaluated the effect of hydrogen charging on high strength Fe-Mn-Al-C steels containing vanadium carbide precipitates using Small Angle Neutron Scattering (SANS) [8]. Figure 2.7 shows the modified incident intensity ($I.Q^2$) vs the scattered intensity (Q) plot. The shoulder observed in the plot is typical of a matrix containing small volume fraction of precipitates. The addition of hydrogen strongly increases the scattering intensity (by approximately 25%). The higher intensity observed after outgassing at 150 °C for 16 hours as compared to the uncharged specimen suggested that some amount of hydrogen was strongly trapped by the precipitates. Under the studied conditions, it was found that approximately 5 ppm wt. of hydrogen was trapped in this way. This effect was not completely reversible upon sample outgassing at 150 °C, indicating that the VC precipitates were moderately stable hydrogen trapping sites.

Laurys et al. compared the trapping of hydrogen by titanium carbide (TiC) and Vanadium Carbide (V_4C_3) precipitates in generic Fe-C-Ti and Fe-C-V alloys respectively [9]. Both materials had semi-coherent precipitates while the sizes ranged from 2-24 nm for TiC and 15-45 nm for V_4C_3. Hot and melt extraction analysis revealed that the total amount of hydrogen was higher in Fe-C-V than in Fe-C-Ti. Diffusible hydrogen contributed to about 70% of the amount of charged hydrogen for Fe-C-V, whereas this contribution was about 30% for Fe-C-Ti (Figure 2.8). Thus, it was concluded that Fe-C-Ti trapped hydrogen more strongly than the Fe-C-V alloy, although a direct comparison of trapping capacity of TiC and V_4C_3 precipitates could not be obtained through these methods.

In a first-principles study on the interaction of hydrogen with TiC precipitates in α- Fe, Di Stefano et al. found that a large variety of possible trapping sites for hydrogen are possible [27]. Such sites can be associated with the particle-matrix interface,

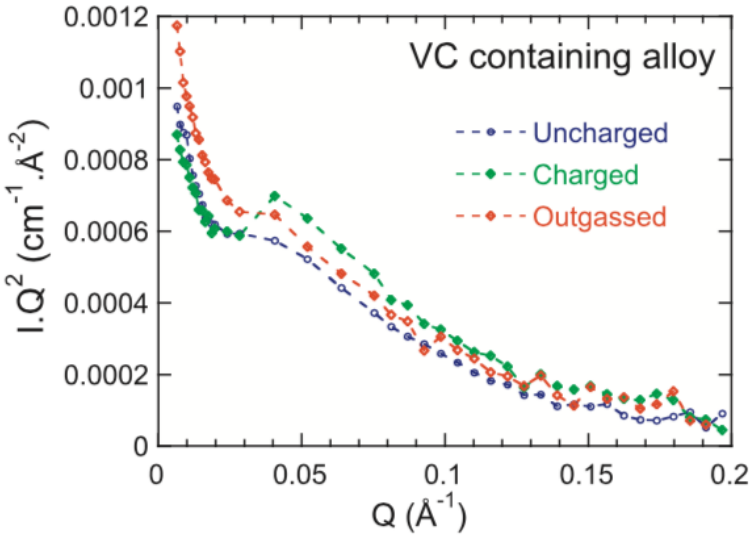

Figure 2.7: Kratky plot of IQ^2 vs Q for different Hydrogen concentrations [8].

misfit dislocation cores and other defects at the interface as well as interstices and carbon vacancies within the precipitate. They found that hydrogen trapping at the semi-coherent interfaces between TiC particles and Fe matrix was moderate; the trap energy was found to range between -0.32 eV for coherent interface segments and -0.50 eV for misfit dislocation cores. Carbon vacancies in the interior of TiC were the strongest traps (-1.09 eV).

In general, it can be concluded that trapping by precipitates can be reversible or irreversible depending upon the structure, stoichiometry and type of precipitate, as well as the type of particle/matrix interface.

2.2.3 Trapping by dislocations

Interactions of hydrogen with dislocations strongly depend on the structures of dislocations. Model structures of dislocations employed for theoretical estimations are often simplified for the convenience of calculation. An atomistic calculation of the distribution and the trap energy of hydrogen around an edge dislocation in iron was conducted by Taketomi et al. [28]. The hydrogen-trap energy was found to be sensitive to both hydrostatic and shear stresses, and strong trap sites were distributed on the slip plane around the dislocation core. The calculated hydrogen-trap energy varied with the type of site and region around the dislocation core with the maximum trap energy lying in the dislocation core.

Actual densities of dislocations in steels that exhibit hydrogen embrittlement are very high and inhomogeneous segments on dislocation lines such as kinks, jogs, tangles and cell configurations induce complex stress and displacement fields. The interaction of hydrogen with dislocations has a direct effect on the plastic flow properties of the material and hydrogen mobility and is one of the key factors for embrittlement via the HELP mechanisms. Further, dislocation movements actually accompany creations of point defects like vacancies and interstitial atoms. In general, dislocations are weak traps and hence may function as mobile carriers for hydrogen, however detailed studies in terms of their contribution to embrittlement is wanting.

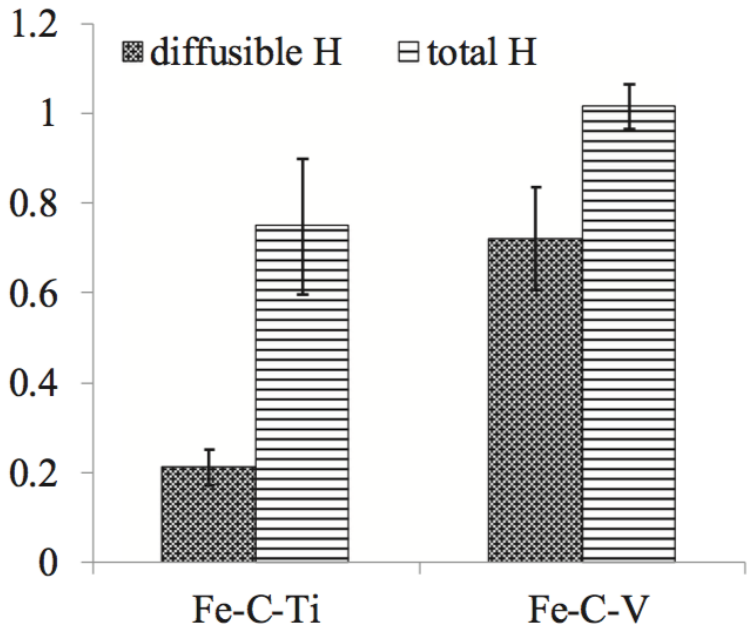

Figure 2.8: Hot and melt extraction results for Fe-C-Ti and Fe-C-V in wppm [9].

2.2.4 Trapping by vacancies

Vacancies can enhance embrittlement through agglomeration according to the HESIV model described previously. they also have high binding energies compared to most alloying elements common in steels. For several metals, a decrease of the vacancy formation energy was observed in the presence of hydrogen, which leads to remarkably high vacancy concentrations. Through first principles calculations on aluminium, it was shown that a large number of H atoms (up to 12) can be trapped at a single vacancy, which overcompensates the energy cost to form the defect [29]. In the presence of trapped H atoms, three nearest-neighbor single vacancies which normally would repel each other, aggregated to form a trivacancy on the slip plane of aluminium, acting as embryos for microvoids and cracks and resulting in ductile rupture along these planes. Moreover, superabundant vacancy formations are known to occur at high pressures and temperatures; in a Pd-H system where vacancy concentrations of about 18% were found [30], and 23% in aluminium[29]. In FCC Fe, it was found that at least six hydrogen atoms can be trapped by a monovacancy, although the formation of a hydride phase was favoured over superabundant vacancy phase [31].

2.2.5 Trapping by grain boundaries

Accumulation of hydrogen along grain boundaries has been revealed directly by means of tritium autoradiography as shown in Figure 2.9 for ferritic steel [10]. Thermal desorption kinetics and tritium autoradiography for ferritic Fe-Ti-C alloys showed that the release of tritium from grain boundaries took place below 300 $^{\circ}C$ and the calculated trapping energy was 59 kJ/mol [32]. The accumulation of hydrogen along grain boundaries does not necessarily induce intergranular fracture. The role of grain boundaries in hydrogen embrittlement is to be considered taking into account various factors - the cohesive strength of boundaries and its modifications by segregated impurities or precipitates as well as concentrated plastic deformation in adjacent areas.

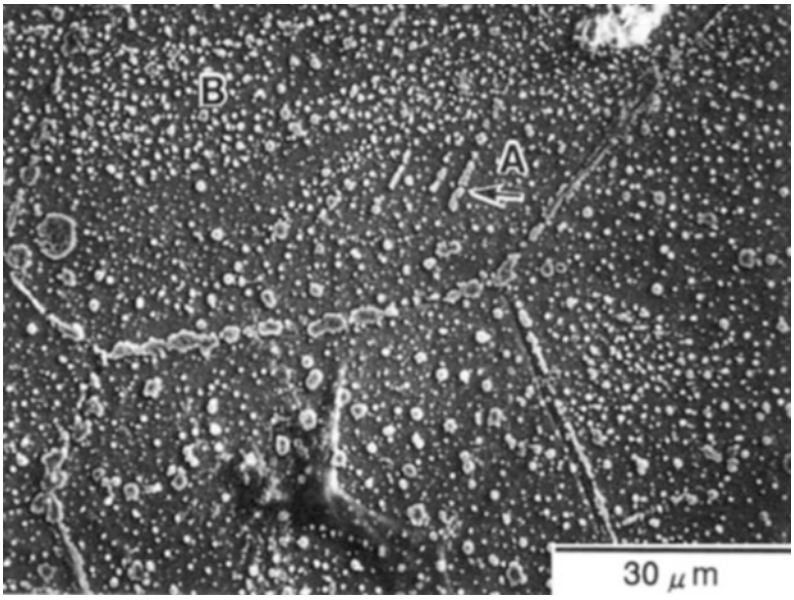

Figure 2.9: Tritium autoradiograph of a ferritic steel tensile strained by 5 % at $-80°C$ [10].

2.2.6 Summary

Hydrogen embrittlement can occur via mechanisms that are specific to the combination of material's microstructure (phases, defects) and environment (stress state, temperature, pressure and hydrogen concentration). Hydrogen diffuses to critical regions in the microstructure, such as crack tips or voids, where it can exert its effects through any of these mechanisms. Microstructural defects play a crucial role in determining the material's susceptibility to hydrogen embrittlement. Defects and second particle phases in the lattice are potential sinks for hydrogen. A freely diffusible hydrogen atom can get trapped at such a sink and remain immobile until sufficient activation energy is made available. The diffusion flux of hydrogen atoms to critical regions is reduced through trapping at these locations. These traps sites can broadly be classified as either reversible (weak) or irreversible (strong) traps. There is no clear distinction between the two, however, weak traps may be activated at ambient temperatures while strong traps desorb at much higher temperatures. The binding energy of hydrogen at a trap site defines the strength of the trap.

Grain boundaries and vacancies are generally weak traps and the hydrogen atom can escape at ambient temperatures. Simultaneously, precipitates and inclusions are strong traps. Trapping at inclusions is detrimental as under high hydrogen activities, the surrounding voids can coalesce into larger voids leading to a decrease in ductile crack growth resistance via the HESIV mechanism. On the other hand, trapping by precipitates can be desirable in regard to improving resistance to HE. The binding energy of a precipitate depends upon its structure and stoichiometry, as well as the nature of particle/matrix interface.

2.3 RESEARCH OBJECTIVES

As is evident from the previous sections, the exact mechanisms responsible for loss of edge ductility in the presence of hydrogen, or any other HE manifestation for that matter, are still an open area for research. However, it is understood that the presence of diffusible hydrogen is the main cause for embrittlement via all of the mechanisms. As an engineering solution to HE, the microstructure may be designed in such a manner so as to have more irreversible traps for hydrogen,

thereby limiting the amount of diffusible hydrogen. The present work is focused on exploring this particular aspect of HE. Titanium and vanadium are two elements which are added for providing grain refinement and solid solution strengthening in micro-alloyed steels [33]. It is speculated that carbide and nitride precipitates of these two elements may be useful in promoting irreversible trapping of hydrogen. The aim of this work is to explore whether trapping by these precipitates leads to a reduction in the amount of diffusible hydrogen and to suggest which of the two elements may be more beneficial in improving resistance to HE. Pertinent research objectives are listed below:

1. To identify which of the above mentioned precipitates is the most efficient trap for hydrogen.
2. To validate the findings from the previous objective by conducting measurements of diffusible hydrogen.

2.4 APPROACH

Density Functional Theory (DFT) based ab-initio calculations have been carried out to examine the energetics of hydrogen in precipitates. Firstly, structure calculations were carried out to determine lattice parameters and phase stability of TiC, VC, VN and TiN. Trap sites in the precipitates were then characterised on the basis of energy of dissolution of hydrogen in these traps. Trapping strengths of carbides and nitrides of titanium and vanadium were compared.

In order to validate the findings from ab-initio calculations, electrochemical methods, namely cyclic voltammetry accompanied with cathodic hydrogen charging have been used to study the absorption of hydrogen. Two steel grades with varying concentrations of titanium and vanadium are used. Cathodic hydrogen charging is employed to load the material with hydrogen while cyclic voltammetry is applied for the detection and measurement of diffusible hydrogen. A comparison between DFT and experimental results is made to determine the contribution of trapping by precipitates towards limiting the amount of diffusible hydrogen.

3 MATERIALS AND METHODS

3.1 MATERIALS AND CHARACTERISATION TECHNIQUES

Two different DP800 steel grades have been used in this study. Their chemical composition is listed in Table 3.1. The compositions were chosen to be quite similar, with mostly notable differences in the concentration of titanium and vanadium. Henceforth, the grade with higher titanium concentration has been referred to as *Grade T* while the other is called *Grade V*. The as received material was hot-dip galvanised. For performing electrochemical experiments, the steel specimens were de-coated.

	Ti	V	C	N
Grade T	0.020	0.004	0.148	45
Grade V	0.009	0.062	0.158	44

Table 3.1: Concentration of titanium and vanadium in the two DP steel grades used in this study. All values are in at %, except N, which is in appm.

SAMPLE PREPARATION: 15mm x 15 mm strips were cut from the two sheets of DP steel grades of thickness 1.3 mm using the Struers Discotom. Cut samples were sanded using sandpaper upto grit 2000, followed by diamond polishing up to a finish of 1 μm. Polished samples were cleansed with iso-propanol in an ultrasonic bath for two minutes. To reveal the grain structure, the samples were then etched with a 2% Nital solution until the surface appeared dull, which took approximately 5 seconds.

The microstructure was characterised using a Leica DMLM optical microscope and JOEL JSM 6500F scanning electron microscope (SEM). Optical and SEM images obtained for both steel grades are shown in Figure 3.1. DP steels have a microstructure of mainly soft ferrite, with islands of hard martensite dispersed throughout. Grain sizes were in the range of 5-10 μm. Carbide precipitates in dual phase steel are known to be in the size range of 4nm up to 50 nm for coherent nano precipitates while incoherent precipitates ranging up to 150 nm have been reported [34, 35]. High Resolution Scanning Electron Microscopy (HRSEM) in combination with Energy Dispersive Spectroscopy (EDS) was used to characterise the precipitates in both specimen. The samples were polished further to a finish of 0.25 μm by using an OP-S suspension. Figure 3.2 shows a precipitate in the size range of 100 nm which was identified with EDS as a complex carbo-nitride of titanium, but the resolution was not high enough to identify smaller precipitates with conviction. Nonetheless, by selecting steel grades with these specific compositions, it was possible to ensure that a high number density of titanium carbides and nitrides would be present in grade T and similarly vanadium precipitates in grade V. Although these are the two classes of precipitates of relevance to this study, several other precipitates such as carbides or nitrides of other alloying elements like niobium as well as oxides and sulphides may be present in the specimen which could interact differently with hydrogen.

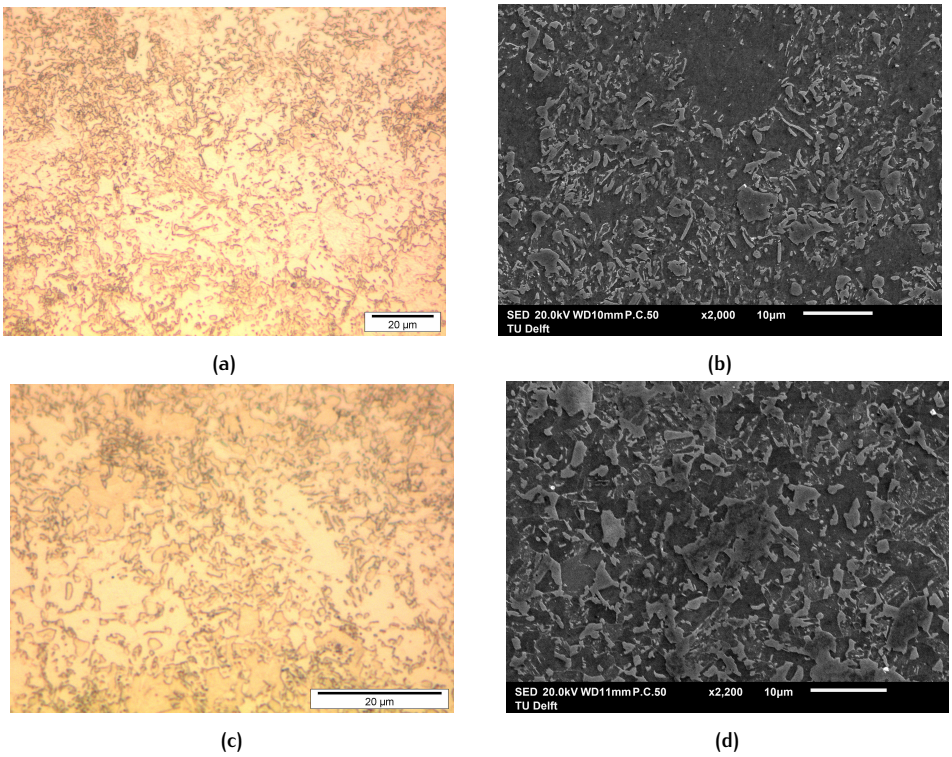

Figure 3.1: (a, c) OM and (b, d) SEM image of grade T and grade V steel respectively

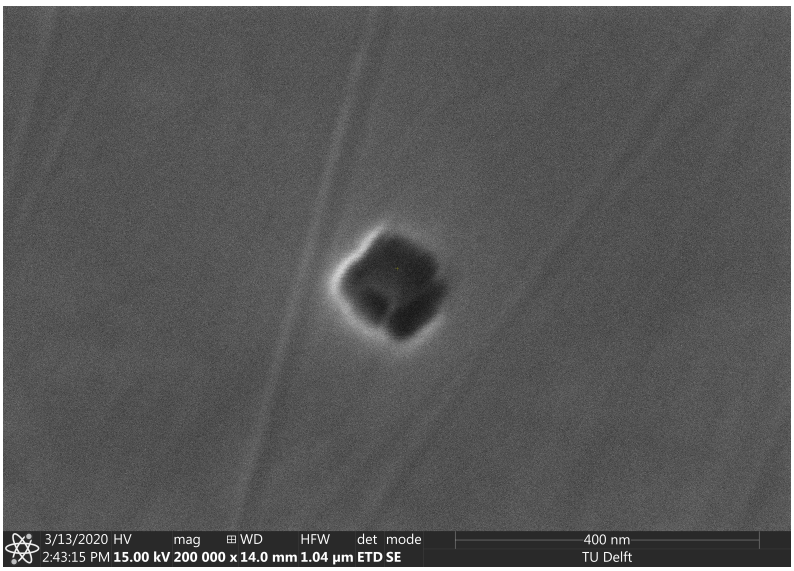

Figure 3.2: HRSEM image of a Ti (C,N) precipitate in grade T steel as identified with EDS

Dual-phase (DP) steels are generally composed of ferrite and 5–20% of martensite with some retained austenite, and their strength ranges from 500 to 1200 MPa. Semi-quantitative XRD analysis of the steel samples revealed a microstructure consisting of 4 ± 1 % retained austenite for both grades. The corresponding XRD patterns are presented in figures 3.3 and 3.4.

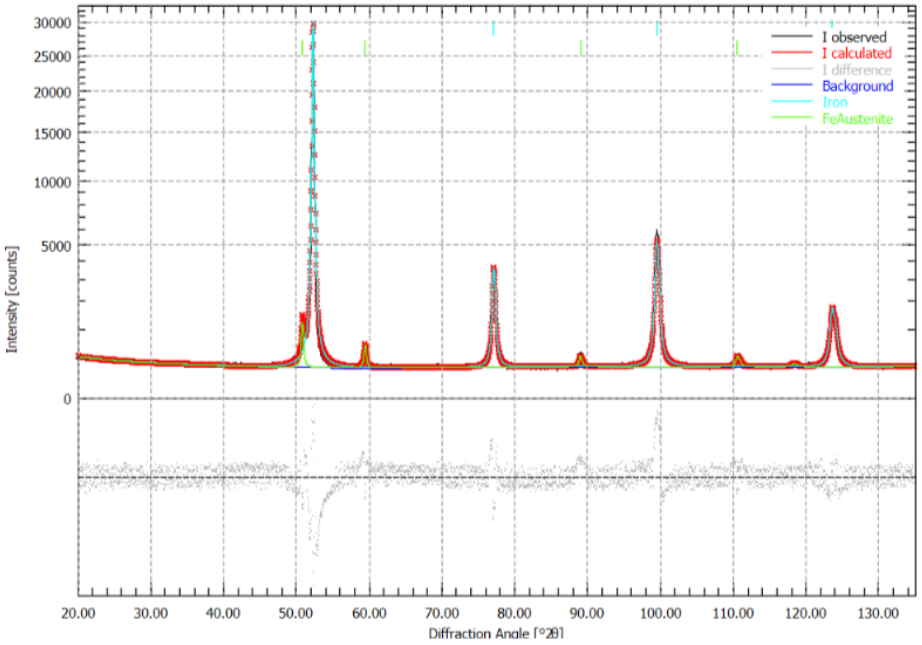

Figure 3.3: XRD sum patterns for grade V steel using Rietveld refinement

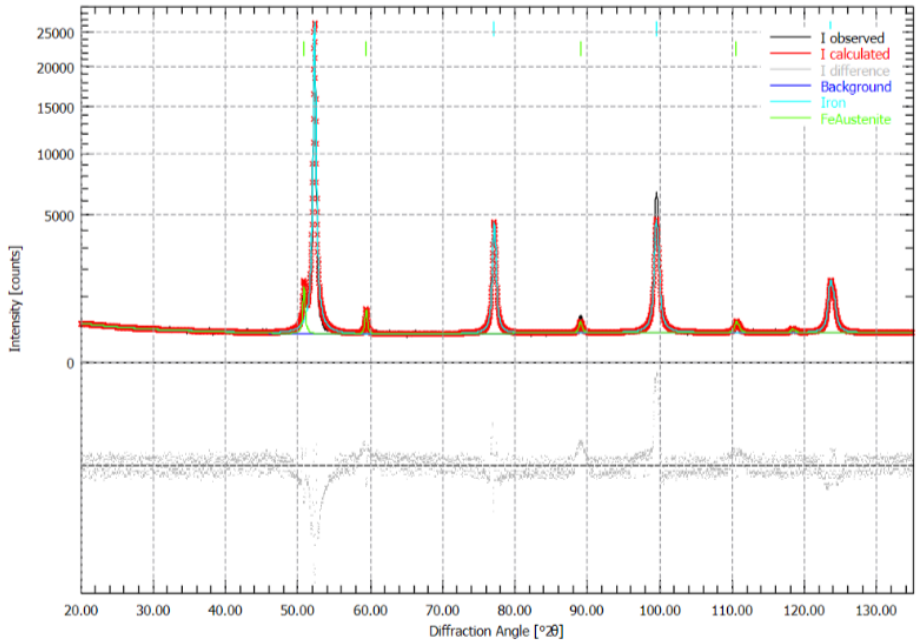

Figure 3.4: XRD sum patterns for grade T steel using Rietveld refinement

As a consequence of performing CV experiments, an oxide layer was formed on the steel surface which possibly contributed to trapping of hydrogen. For the purpose of characterising the oxide layer, FTIR tests were performed on the samples post CV experiments. As molecules exhibit specific IR fingerprints, any molecular bonds that would have been formed between the oxide and hydrogen could

be detected. Thermo-Nicolet Nexus FTIR apparatus equipped with a mercury-cadmium-telluride liquid-nitrogen-cooled detector and a nitrogen-purged measurement chamber was used for this purpose. Steel specimen polished up to a finish of $1\mu m$ were used for generating a baseline. The baseline was subtracted from the spectra of hydrogen charged and uncharged samples. FTIR results are presented alongside CV results in Chapter 4.

3.2 SIMULATION METHODS

In Materials Science, ab-initio methods are capable of providing insights into the fundamental nature of interaction between atomic species and help to fill in the gaps in our understanding of observable phenomena. In this work, the capability of carbides and nitrides of titanium and vanadium to bind hydrogen was investigated by performing electronic structure calculations using first principles within the framework of DFT.

3.2.1 Background

Analogous to Newton's laws of motion and conservation of energy which describe the behaviour of a body in a classical system, Schrödinger's equation predicts the behaviour of elementary particles in quantum mechanics which acknowledges the wave particle duality of all matter. The time independent form of this equation describes the energy of stationary states and is given in Equation 3.1.

$$\nabla^2\psi + \frac{8\pi^2 m}{h^2}(E - V)\ \psi(x, y, z) = 0. \tag{3.1}$$

The equation is often simplified further as $E\psi = \mathcal{H}\psi$. This simple looking equation is immensely powerful and governs the properties of all matter at ambient conditions. For a system comprising of N electrons, ψ is the 3N dimensional wavefunction, and E and V represent the total energy and potential energy of the system respectively. ∇^2 is the Laplacian, which takes the form $\frac{\partial^2}{\partial x^2} + \frac{\partial^2}{\partial y^2} + \frac{\partial^2}{\partial z^2}$ in three dimensions. The term $\nabla^2\psi$ thus represents the kinetic energy of the system under consideration.

The potential energy V is the sum of interactions between the nuclei, between the nuclei and electrons, as well as through the interaction between electrons. A simplification is made through the Born-Oppenheimer approximation, which treats the nuclei as stationary as compared to the electrons. This is a valid approximation, as the mass of a proton is 1836 times that of an electron. The interaction between the electrons and nuclei is then simply the coulumbic interaction between the electrons and stationary charge from the nuclei. The second term in the potential energy, arising from electronic interactions is considered to be the holy grail in electronic structure calculations; several methods have been tested to derive this interaction potential.

To find solutions to Equation 3.1, one must find the set of wavefunctions ψ which satisfy the equality. The ground state wavefunction and energy may be found by searching all possible wavefunctions for the one that minimises the total energy. This is a rather complex mathematical problem as the electron wavefunction is a multidimensional object that explicitly couples the motion of all particles and solving Equation 3.1 requires treatment of a 3N dimensional partial differential equation. In the late 1920s, Hartree was among the first to realize that the newly derived

Schrödinger equation could be solved for multi-particle systems if the wavefunction is approximated by a product of single particle wave functions.

$$\psi(r_1, r_2, ..., r_n) = \phi_1(r_1)\phi_2(r_2)...\phi_n(r_n). \tag{3.2}$$

Physically, the Hartree wavefunction implies that each electron moves independently in the electrostatic field created by all of the others. The Hartree equation did not take into account the antisymmetry required by Pauli's exclusion principle. This was rectified by Fock by considering the determinant form of Equation 3.2.

$$\psi(r_1, r_2, ..., r_n) = \frac{1}{\sqrt{n!}} \begin{vmatrix} \phi_1(r_1) & \phi_2(r_1) & .. & \phi_n(r_1) \\ \phi_1(r_2) & \phi_2(r_2) & .. & \phi_n(r_2) \\ : & : & : & : \\ : & : & : & : \\ \phi_1(r_n) & \phi_2(r_n) & .. & \phi_n(r_n) \end{vmatrix} \tag{3.3}$$

Substituting this in Equation 3.1 and treating the electron-nuclei and electron-electron interactions separately in the potential energy term yields the Hartree Fock equation,

$$\begin{aligned} E_n\phi_n(r) = &\left[-\frac{1}{2}\nabla^2 + \hat{V}_{ext}(R_I, r) + \hat{V}_H(r) \right]\phi(r) \\ &- \sum_m \int dr' \frac{\phi_m^*(r')\phi_n(r')}{|r' - r|}\phi_m(r) \end{aligned} \tag{3.4}$$

where $\hat{V}_H(r)$, the Hartree potential given by $\int \frac{n(r')}{|r'-r|}dr'$, is the coulumbic interaction of an electron with the average electron density and $\hat{V}_{ext}(r)$ is the interaction of an electron with the nuclei. The additional term in Equation 3.4 is the exchange potential which arises from the repulsion of electrons with like spin.

This effective one particle wave equation may be solved in a self consistent loop, which lends the Hartree-Fock method. The solution of Hartree-Fock equation is not exact, because the true wave function is not a product of two orbitals, but is rather a complicated function of both variables simultaneously. The difference between a molecule's HF energy and its exact energy is the correlation energy E_c and the challenge of its determination is known as the "electron correlation problem" and has been the focus of ongoing research efforts for almost a century. Several methods have been used to estimate this correlation energy; these fall under two broad categories: wavefunction based methods and density based methods. A detailed account of these can be found in [36]. Although the Hartree–Fock (HF) model neglects the inter- electron correlations that influence chemically important phenomena such as bond making and breaking, electron gain and loss, and the response of a molecule to an external electric and/or magnetic field [36], it is the central starting point for most methods that describe the many-electron system more accurately.

DENSITY FUNCTIONAL THEORY has been immensely successful in making electronic structure calculations in solid state physics and quantum chemistry. The appeal to this method lies in the fact that larger systems can be treated as compared to traditional ab-inito methods while retaining much of their accuracy at low computational costs. In DFT, the energy is written as a function of electron density which in turn is a function of position and hence the energy is a functional of electron density. Early density functional theories include independent treatments by Thomas and Fermi in 1927. They assumed that the potential energy term in Equation 3.1 comprises of the coulumbic attraction between the electrons and nuclei and repulsion between electrons. They further assumed that the potential energy and the kinetic energies of electrons could be written as functions of the electronic density of the system. The TF model speculates that the electron density in a system

varies slowly in the scale of electronic wavelengths so that many electrons may be localised within a volume over which the density changes by a small fraction of itself. In this manner, the kinetic energy was approximated by the energy of a uniform electron gas with density ρ according to equation 3.5,

$$T[\rho] = C_F \int \rho^{5/3}(r)dr \tag{3.5}$$

where $C_F = (3/10)(3\pi^2)^{2/3}$.
The expression for the potential energy according to this model is shown in equation 3.6, where the first term is due to pairwise electronic repulsion while the second term is the attraction between the electrons and nuclei.

$$J[\rho] = \frac{1}{2} \iint \frac{\rho(r_1)\rho(r_2)}{|r_2 - r_1|} dr_1 dr_2 - Z \int \frac{\rho(r)}{r} dr \tag{3.6}$$

This expression for potential energy neglects any correlation between the electrons. A first *correction* was made by Dirac in 1930 who modified the TF model by including the exchange energy. This takes into account the fact that two electrons with same spin cannot occupy the same position (similar to the Hartree-Fock method). The difference in energy between parallel spin and anti parallel spin couples is the exchange energy and was expressed mathematically by Dirac as Equation 3.7,

$$E_x[\rho] = C_x \int \rho^{4/3}(r)dr \tag{3.7}$$

where $C_x = (3/4)(3/\pi)^{1/3}$.
Both TF and TFD models overestimate the binding energy of electrons. The major error in the TF approach comes from approximating the kinetic energy as a density functional. Moreover, the notion that the ground state energy can be expressed as a function of electron density was purely conjectural at this point.

The most significant leap in density functional theory came about with the formulation of the Hohenberg Kohn theorem and subsequent Kohn Sham equations. In 1964, Hohenberg and Kohn formulated a set of theorems which ensured that the exact ground state energy of a system can be calculated, without recourse to the Schrödinger equation, from a variational principle involving only the electron density, i.e., the chain of correlations can be disentangled completely, at least in principle . The total energy of the system subjected to an external potential V is given by

$$E[n(r)] = F_{HK}[n(r)] + \int \hat{V}_{ext}(r)n(r) \tag{3.8}$$

where F_{HK} is a functional of the electron density n which is a function of position r. The HK theorem consists of a set of three statements:

- All observable ground state properties of a system are unique functionals of the exact ground state density.
- The energy functional is variational, meaning that the exact ground state density can be determined by minimization of the energy functional.
- The functional F_{HK} is universal.

The functional F_{HK} comprises of the kinetic energy, hartree energy and all contributions from inter electron interactions.

$$F_{HK}[n(r) = E_K[n(r)] + E_H[n(r)] + E_{XC}[n(r)] \tag{3.9}$$

The term E_{XC} is the exchange correlation functional and contains all the uncertainties in the exact solution for energy. The exact form of this universal functional is unknown, however, E_{XC} includes the exchange energy, correlation energy and the error in kinetic energy arising from the assumption of a non interacting system. The simplest approximation for estimating E_{XC} is to assume that the density can be treated locally as a uniform electron gas; the exchange correlation energy at each point in the system is the same as that of an uniform electron gas of the same density. Such a model for E_{XC} is known as the Local Density Approximation (LDA). An improvement in the accuracy provided by the LDA can be obtained by Generalised Gradient Approximation (GGA) functionals. Gradient corrected or GGA functionals depend on the local density as well as on the spatial variation of the density.

3.2.2 Details of the calculation

All DFT calculations were carried out using the Vienna Ab-initio Simulation Package (VASP) [37, 38]. The generalized gradient approximation (GGA) as given by Perdew, Burke, and Ernzerhof [39] was employed for exchange correlation. The Methfessel - Paxton method [40] with a smearing width of 0.15 eV has been used for the Fermi surface smearing. The single-electron wave functions have been expanded by using plane waves up to an energy cutoff of 500 eV. All lattice vectors and atomic positions were relaxed until the residual forces acting on each atom were below 0.01 eV/Å. An energy tolerance of 10^{-6} eV was defined as a convergence criterion for the self-consistent electronic loop. The Brillouin zone was sampled using Monkhorst-Pack grids [41] with a 24x24x24 grid for the 8 atom unitcell and 6x6x6 grid for the 64 atom supercells. All calculations were carried out as spin-polarized.

3.3 ELECTROCHEMICAL METHODS

3.3.1 Background

In order to investigate hydrogen embrittlement through experimental methods, the test material must be exposed to a hydrogen rich environment. This can be achieved by subjecting the sample to either a gaseous hydrogen environment or to an aqueous environment in which hydrogen is generated electrochemically. The electrochemical approach has the advantages that charging conditions can be varied more precisely and higher hydrogen activities at the sample surface can be established. Moreover, there is no requirement for specialised apparatus which makes it a handy method for conducting small scale experiments. While both these approaches have been used fairly consistently for studying HE in steels, reports on the correlation between the materials response to each condition are lacking. The best approach is one which simulates the actual environment that the material would be subjected to during its service life.

The difficulties in obtaining experimental observations of hydrogen in the microstructure and hydrogen absorption in general has led towards the application of atypical methods for studying HE. Such methods need to be reliable, reproducible and most importantly, feasible. Several electrochemical techniques have been employed to measure the dissolution of hydrogen in metal lattice. Permeation based methods are useful in providing information on the diffusivity and solubility of hydrogen in metals. An example is the Devanathan Stachurski cell [42], which is in fact sold commercially for the sole purpose of measuring hydrogen permeation. In this method, hydrogen is permeated through thin membranes of the test material. One side of the membrane is subjected to the cathodic treatment, and a small

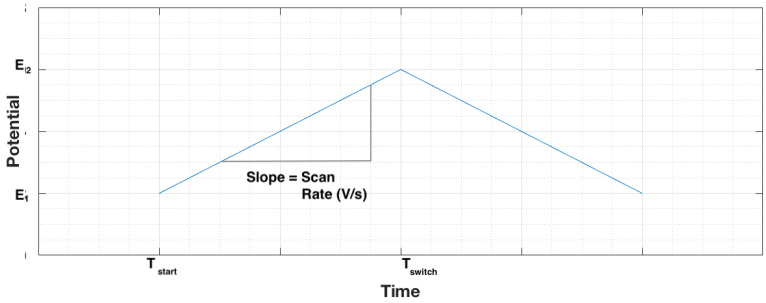

Figure 3.5: Potential waveform applied to the working electrode during cyclic voltammetry

fraction of the simultaneously formed hydrogen atoms pass through the membrane which are collected on the opposite side. The permeation can thus be measured which yields information on the diffusivity of hydrogen through the membrane. Permeation methods have also been used to estimate trap density in the metal lattice [43, 44]. Potential based methods such as cyclic voltammetry and potentiostatic oxidation have also been applied for measuring hydrogen sorption. The concentration of diffusible hydrogen in materials subjected to hydrogen charging conditions can be determined with these methods. The above mentioned techniques can be integrated seamlessly with electrochemical hydrogen charging which means that there is no time lag between the hydrogen uptake and measurement steps. This is particularly advantageous when dealing with a highly diffusible element such as hydrogen. Ozdirik et. al. reported a 90% loss of Hydrogen absorbed in plain carbon steel within 100 seconds during which the test sample was removed from the charging cell and placed in the hot extraction furnace [45].

CYCLIC VOLTAMMETRY is an electrochemical technique which is most commonly used to investigate redox processes. The experiment involves applying a potential to the working electrode which changes with time as shown in Figure 3.5. The current flowing through the working electrode is recorded as a function of the electrode potential. The area under the current versus potential plot can be integrated to obtain the net quantity of charge and consequently the number of electrons participating in the redox process. As shown in figure 3.5, the potential of the working electrode begins at E_1 which is usually selected so that the chemical species under investigation are not initially oxidised or reduced. The potential is then swept in a linear manner to a voltage, E_2, at which point the direction of the scan is reversed. The potential interval (E_2 - E_1) is chosen such that the oxidation or reduction process of interest lies in this interval.

For a redox process, the concentration of oxidized and reduced halves of the redox couple are related to the electrode potential, E, by the Nernst equation.

$$E = E^0 + \frac{RT}{nF}\, ln\, \frac{[Ox]}{[Red]} \tag{3.10}$$

where E^0 is the formal reduction potential of the redox couple, R is the universal gas constant, n is the number of electrons transferred during the redox event, F is Faraday's constant and [Ox] and [Red] represent the concentrations of the oxidised and reduced species respectively. When an external potential is applied to the electrochemical cell, the concentration of oxidised and reduced species changes according to the Nernst equation until an equilibrium is achieved. The exchange of electrons during this process leads to a current being generated in the cell. A plot of the resulting current against cell potential is known as a voltammogram. Considering a simple electrode process of the form $A + e \Longleftrightarrow B$, where A and B are

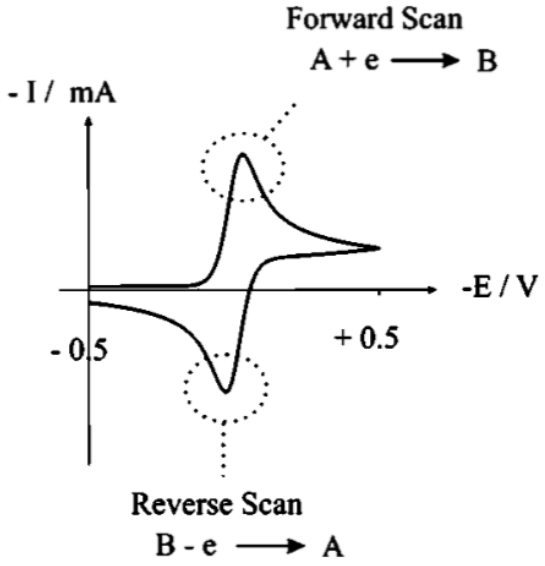

Figure 3.6: Simulated voltammogram wave shape for a simple redox process [11].

species in the solution phase, the shape of the voltammogram then depends on the following factors [11]:

- The standard electrochemical rate constant and the formal potential of the A/B couple.
- Diffusion constants of A and B.
- The voltage sweep rate and the potential range E_2 - E_1.

Figure 3.6 shows a simulated cyclic voltammogram for the reduction of A to B. It can be seen that at relatively positive potentials, no current flows through the cell as the electrode is insufficiently negative for reduction to occur. As the potential is swept further towards negative values, the current rises as a consequence of flow of electrons that participate in the reduction process. Subsequently, the current reaches a maximum value and begins to drop. This formation of a peak in the current curve is a consequence of the build up of a diffusion layer at the electrode-solution interface which prevents further exchange of ionic species. Once the electrode potential has reached a value at which the surface concentration of A is close to zero, the current decays approximately as $1/\sqrt{t}$. At E_2, the direction of the potential sweep is reversed and an oxidation peak is similarly formed.

The evolution of hydrogen during cathodic charging is also an electrochemical process according to Equation 2.2. Correspondingly, CV has been employed for studying the absorption of hydrogen in steels [25, 45]. Figure 3.7 shows voltammograms obtained for a grade V steel sample. The sample was subjected to two initial scans followed by 30 minutes of cathodic hydrogen charging. Finally, two more scans were done post charging. The details of the test conditions and data interpretation are presented in the following sections. However, it can be seen from the initial scans that there are two distinct peaks indicating that two separate redox processes are occurring during this potential sweep. Immediately after charging, an additional peak, overlapped with the first peak is formed. To identify the redox reaction which is responsible for a particular peak, a Pourbaix diagram may be utilised. A Pourbaix diagram plots the equilibrium potential (Ee) between a metal and its various oxidised species as a function of pH. Essentially, it is a phase diagram that maps the conditions of potential and solution pH where different redox species are stable. Peak attribution using Pourbaix diagrams are discussed in detail

in Section 4.2.1.

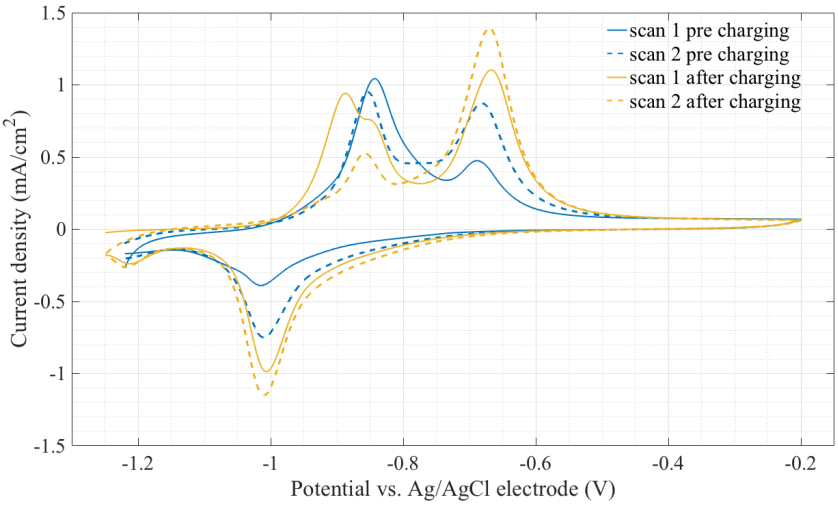

Figure 3.7: CV voltammograms for DP800 steel specimen subjected to 30 minutes of cathodic hydrogen charging

For quantifying the desorbed hydrogen from CV, different approaches have been utilised. The most commonly used method is one in which the amount of hydrogen is calculated corresponding to the hydrogen peak obtained in the first CV scan post hydrogen charging [25, 46]. The hydrogen peak is firstly delineated from any overlapping peaks and the area under the peak calculated. This area is in the units of $A.V.cm^{-2}$. This is transformed into the surface charge density by dividing with the voltage sweep rate. With the knowledge of surface charge density, the number density of electrons participating in charge transfer can be found out. This is represented in equations 3.11 and 3.12. As each hydrogen atom reacts with one electron during the oxidation / reduction process, the number of hydrogen atoms desorbed is equal to the number of electrons.

$$\rho_s = \frac{peak\ area}{potential\ sweep\ rate} \tag{3.11}$$

$$\left[\frac{C}{cm^2}\right] = \left[\frac{A.cm^{-2}.s}{vs^{-1}}\right] = \left[\frac{A.V}{cm^2}\right] \tag{3.12}$$

The amount of hydrogen calculated in this manner is dependent on the scan rate in this method, as well as the choice of potential range. To overcome these issues, the first CV step after charging may be replaced by a potentiostatic discharging step in the hydrogen is desorbed by appying a constant potential which corresponds to the electrode potential of hydrogen evolution under the specified conditions [45]. At this potential, hydrogen ions on the steel surface are reduced leading to a continuous rise in current until all the available hydrogen is reduced. The resulting current time plot can be directly integrated to obtain the charge density and subsequently the number density of hydrogen atoms may be found.

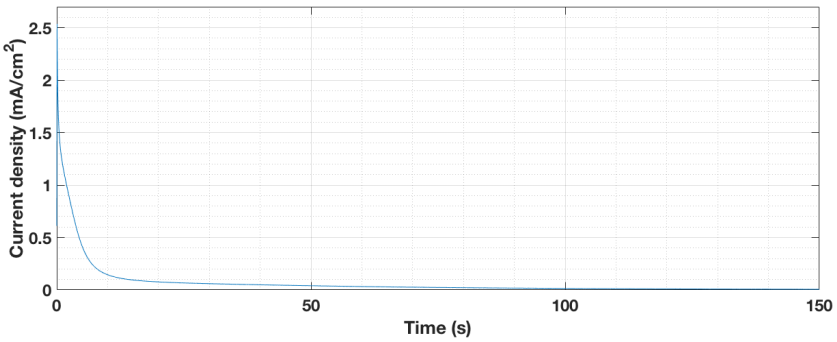

Figure 3.8: Current time transients obtained after discharging at potential of -0.9V vs Ag/AgCl for 30 minutes.

3.3.2 Procedure

SAMPLE PREPARATION: Samples of thickness 15 mm x 15 mm x 1.3 mm were de-coated by immersing in 1:1 HCl solution followed by rinsing with isopropanol. One side of the sample, which was to be exposed to the electrolyte was sanded and polished to a surface finish of $1\mu m$.

ELECTROCHEMICAL CELL SET-UP: Electrochemical measurements were performed in a one-compartment acrylic cell. The electrolyte was a 1M NaOH solution containing 8g/L of Thiourea and fresh electrolyte was used for each test. The pH of this solution was in the range of 12.8-13.3. Thiourea is an organo-sulfur compound with the formula $SC[NH_2]_2$ and is known to function as a recombination position; it facilitates the retention of protons in the electrolyte during the test thereby promoting the ability of atomic hydrogen to enter steel. A double junction Ag/AgCl electrode filled with saturated KCl solution was used as reference electrode; the filling solution was renewed periodically to minimse the effect of contamination. A platinum wire mesh was used as the counter electrode. A circular area of 0.385 cm^2 on the sample was exposed to the electrolyte. The experiment was controlled with a Bio-Logic VSP-300 potentiostat. The cell set-up used is shown in Figure 3.9 along with a schematic of the three electrode cell configuration.

In such a set-up, the working electrode (WE) corresponds to the metal specimen that is cathodically polarised so that hydrogen evolution takes place on the surface of this electrode. Reference electrode (RE) is utilised to provide a stable reference point against which the potentials of other electrodes are measured. The counter electrode (CE) is a non-reactive material (usually platinum) that completes the circuit allowing the electrons to flow.

TEST PARAMETERS: The test consisted of three steps:

1. Two initial cyclic voltammetry scans: The first scan was done to ensure that the sample surface was consistent for all tests, while the second scan was used to generate a baseline.

2. Immediately after the second CV scan, a hydrogen charging was carried out by applying a constant potential of -1.25 V vs Ag/AgCl. In this step, the electrolyte was oxidised to generate H^+ ions on the steel surface. Charging was done for three different durations of 30, 60 and 120 minutes.

3. For quantifying the amount of hydrogen, a static potential of -0.9V vs Ag/AgCl was applied to the cell after hydrogen charging, instead of a CV scan.

4. Immediately following hydrogen charging, cyclic voltammetry scans were repeated.

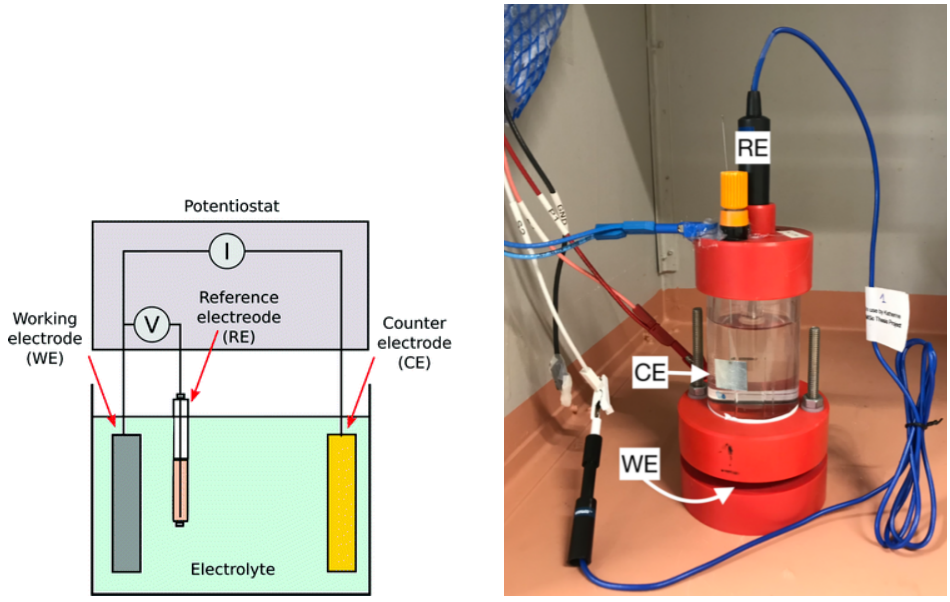

(a) (b)

Figure 3.9: A schematic of the three-electrode cell (a) and the set-up used in this study (b). The sample is clamped between the two bottom plates with a circular area of 1 cm diameter being exposed to the electrolyte.

Three sets of tests was performed for each grade. All test parameters are listed in Table 3.2.

Step	Electrolyte	Potential (V)(Ag/AgCl)	Duration (minutes)	Scan Rate (mV/s)
Initial CV		-1.25 to -0.2	-	10
H charging	1M NaOH + 8g/L Thiourea	-1.25 V	30, 60 , 120	-
Final CV		-1.25 to -0.2	-	10
H discharging		-0.9	30	-

Table 3.2: Parameters for cyclic voltammetry experiments

4 RESULTS AND DISCUSSION

4.1 FIRST PRINCIPLES CALCULATIONS FOR HYDROGEN TRAPPING IN PRECIPITATES

Both titanium carbide and vanadium carbide crystallize in the rock salt crystal structure. The characteristics of their precipitation in steels, including the size, morphology and composition, depend upon the heat treatment parameters yet vanadium carbide precipitates in steel are known to be off stoichiometric [47, 48].

4.1.1 Structural parameters and energies

The equilibrium lattice parameters obtained for vanadium carbide and titanium carbide were 4.155 Å and 4.33 Å respectively. The enthalpy of formation of these compounds were calculated as the difference between the total energy of the compound phase and that of its constituent elements. Equation 4.1 depicts this relation, where M is the metal atom, X is a carbon or nitrogen atom and a and b are the stoichiometric coefficients of the two constituents of the compound.

$$H_f(M_aX_b) = [E(M_aX_b) - aE(M) - bE(X)] \tag{4.1}$$

Table 4.1 displays the formation enthalpies of titanium carbide, titanium nitride, vanadium carbide and vanadium nitride along with the lattice parameters. *H-f* for all compounds was independent of super cell scaling. The values obtained are comparable with other reports. [49, 50, 51, 52] and the references used therein. The formation of each compound, except vanadium nitride, is exothermic indicating the phases are stable. In the case of vanadium nitride, it is known through diffraction studies that the cubic rock-salt type structure transforms into a tetragonal modification at temperatures below 205 K [53].

Compound	$a_0(\AA)$	H_f(eV)
VC	4.15	-3.07
TiC	4.33	-7.69
VN	4.12	5.16
TiN	4.25	-2.17

Table 4.1: Lattice parameters and formation enthalpies of various compounds

VACANCY FORMATION ENERGIES were calculated according to Equation 4.2, where ${\mu^0}_X$ is the energy of the reference state for X (C or N), the choice of which has a significant impact on the calculated values. In the present work, ${\mu^0}_X$ is taken as the ground state energy of graphite (X = C) or half the energy of a nitrogen molecule (X = N). The energy calculated according to 4.2 represents the energy gained or lost by removing a carbon/nitrogen atom from the lattice.

$${E^v}_f = E[MX_{vacancy}] - E[MX_{perfect}] + {\mu^0}_X \tag{4.2}$$

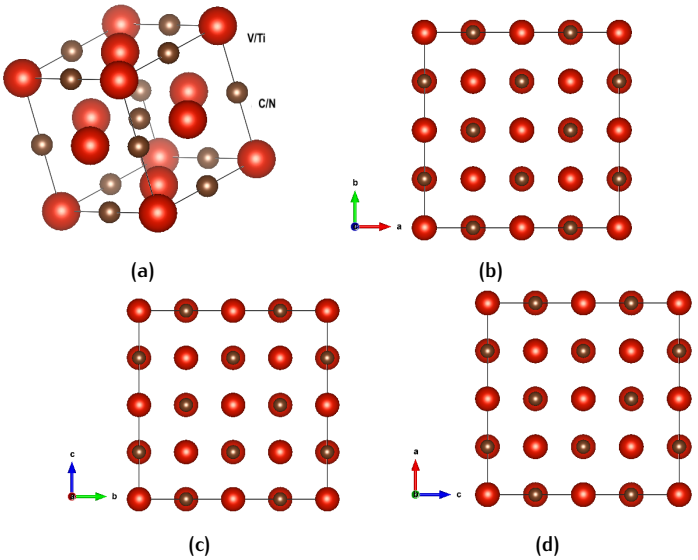

Figure 4.1: Crystal structure of VC/VN or TiC/TiN: (a) unit cell and (b, c, d) 2x2x2 supercell used for calculations. Red spheres are metal atoms and brown ones are carbon/nitorgen.

Vacancy formation energies for the 8-atom unitcell and 64-atom supercells are listed in Table 4.2. The 1x1x1 supercell significantly overestimates the vacancy formation energy. Among the four compounds, carbon vacancy formation in titanium carbide is endothermic, suggesting that the formation of a carbon vacancy in titanium carbide is energetically unfavourable. On the other hand, vacancy formation in titanium carbide and both vanadium carbide and nitride is exothermic. This finding is supported by the experimental observation of off stoichiometry in VC, which is commonly reported to precipitate as V_4C_3 or V_6C_5 [54]. However, carbon vacancies in titanium carbide are also experimentally observed at finite temperatures. The calculated value for TiC is close to zero, hence when TiC is grown at sufficiently high temperatures so as to overcome the activation barrier, vacancies can nevertheless form, and the statistics will follow a Boltzmann distribution.

Supercell size	**VC**	**TiC**	**VN**	**TiN**
1x1x1	1.06	1.81	-1.87	0.33
2x2x2	-0.81	0.73	-2.33	-0.64

Table 4.2: Vacancy formation energy in eV.

4.1.2 Hydrogen trapping by carbides and nitrides

The energy of dissolution of hydrogen in bulk phases is defined by the difference between the total energy of the precipitate-hydrogen complex and that of a bulk phase with no hydrogen and a separate hydrogen atom (Equation 4.3). The formation enthalpy of hydrogen (μ_{H_2}) is calculated as half of the ground state energy of a H_2 molecule.

$$H_f(M_aX_bH) = E(M_aX_bH) - E(M_aX_b) - \frac{1}{2}\mu H_2 \tag{4.3}$$

Hydrogen solution energies in the studied compounds were calculated at the interstitial sites. As the octahedral sites are fully occupied by C or N atoms, only the tetrahedral sites can offer a stable binding to H atoms. The binding energies

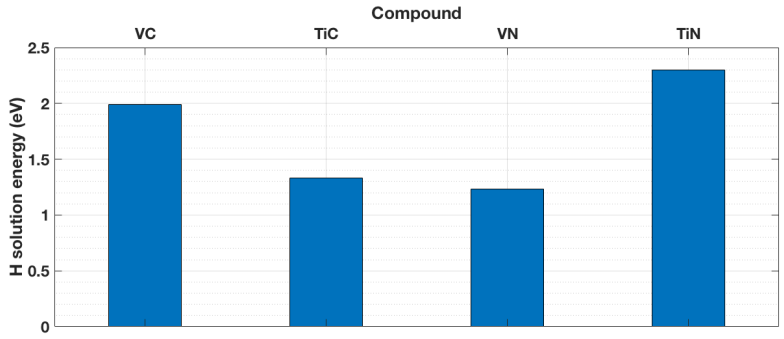

Figure 4.2: Hydrogen solubility in interstitial sites as calculated using Equation 4.3

are shown in Figure 4.2. The dissolution of hydrogen in tetrahedral interstices is endothermic in all cases. Thus, for dissolution in interstices, the hydrogen atom must overcome an activation barrier.

The energy of hydrogen dissolution in a C/N vacancy within the precipitate was also calculated according to Equation 4.3 and the values for the four compounds are plotted in Figure 4.3. Hydrogen solution enthalpy is negative for all compounds, indicating exothermic dissolution of hydrogen in vacancies. Comparison with Figure 4.2 suggests that vacancies within a precipitate are energetically more favourable for a hydrogen atom as compared to tetrahedral interstices. A carbon vacancy in titanium carbide is seen to have a strong affinity for hydrogen. Hydrogen solution enthalpy in a vacancy in titanium carbide was -0.91 eV while that in vanadium carbide was -0.06 eV, with the nitrides lying in between this range.

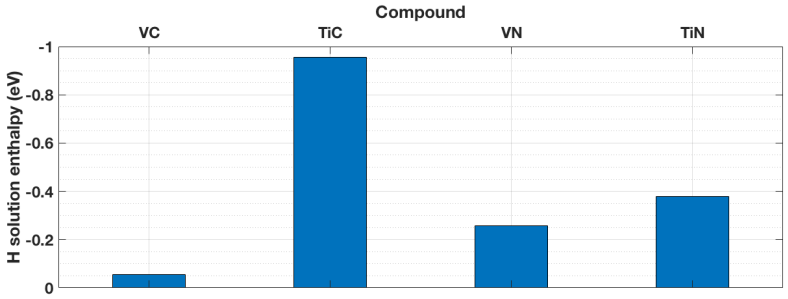

Figure 4.3: H solution energy in carbon or nitrogen vacancies as calculated from Equation 4.3

The expressions 4.3 and 4.2 may be combined to yield the vacancy-hydrogen complex formation energies. This parameter represents energy required for the formation of a vacancy and subsequent trapping of hydrogen in the vacancy. The vacancy-hydrogen complex formation energies calculated for 2x2x2 supercells are plotted in Figure 4.4. The vacancy-hydrogen complex formation energy for vanadium carbides was -0.89 eV and that of titanium carbide was -0.22 eV. Owing to the off-stoichiometry, vanadium carbide appears to be a stronger hydrogen trap than titanium carbide at zero temperature. Vanadium nitride was also similarly found to be a stronger hydrogen trap than titanium nitride (-2.6 eV versus -0.1 eV). It must be noted that complex carbo-nitride phases are also known to precipitate in steels; H trapping in such precipitates would depend on their crystal structure and stoichiometry.

Finally, the trapping energy for hydrogen was calculated as the difference between the H solution enthalpy in the precipitate (both interstitial and vacancy) and

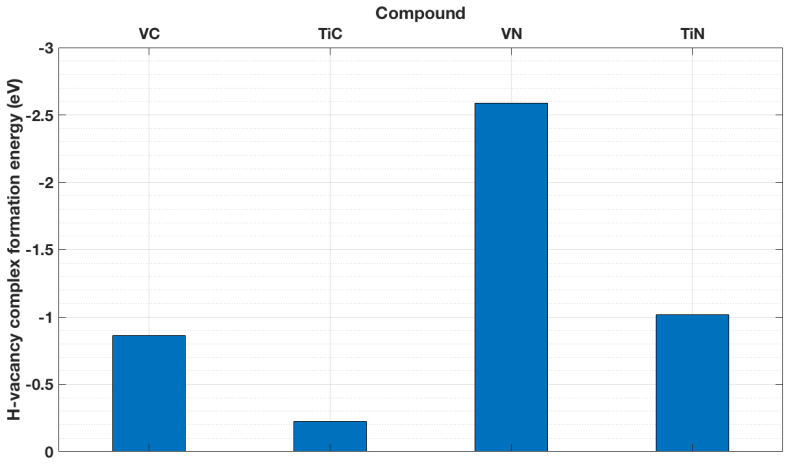

Figure 4.4: Hydrogen-vacancy complex formation energy for 2x2x2 supercells

the solution enthalpy in surrounding ferrite matrix. This is again a theoretical value, which is useful for comparing the trapping capability of the various precipitates. Trapping capability was found to be in the following order: TiN interstitial < VC interstital < TiC interstital < VN interstital < TiC vacancy < VC vacancy < TiN vacancy < VN vacancy. Overall, vanadium precipitates were found to be stronger traps than those of titanium.

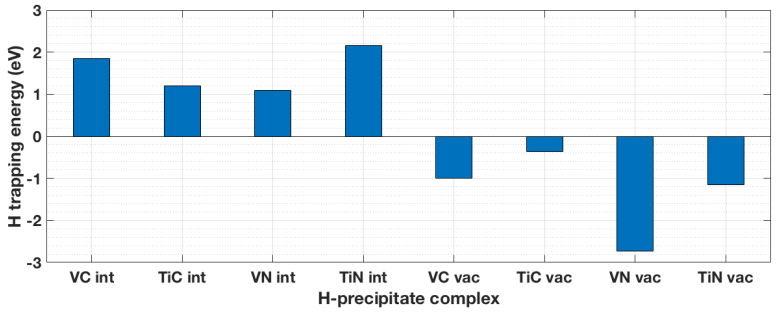

Figure 4.5: Trapping energy with respect to the ferrite matrix

4.2 HYDROGEN SORPTION

4.2.1 Peak attribution and detection of absorbed hydrogen

The Pourbaix diagram for iron is shown in Figure 4.6. At a pH range of 12.8-13.3, iron is stable up to a potential of -1.2 V (Potential is measured against a standard hydrogen electrode in this case). Sweeping the potential further towards positive values leads to the oxidation of iron to FeO and Fe_2O3. The oxidation of Fe to Fe2O3 occurs around -0.55 V (-0.75 V vs Ag/AgCl). The lower orange line marks the beginning of the region above which hydrogen ions from the solution are reduced. In the pH range of interest, this lies at a potential of around -0.7 V (-0.9 V vs Ag/AgCl). These two potential values are highly relevant to the discussion on CV results.

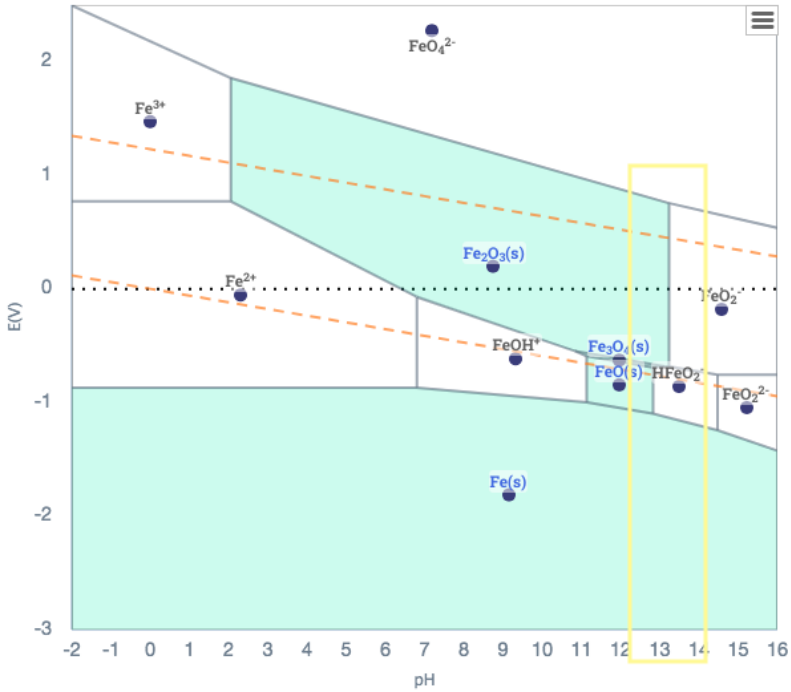

Figure 4.6: Pourbaix diagram of iron. The yellow rectangle marks the pH range of the electrolyte used in this study and the dashed orange lines represent the stability region of water. The filled regions in the diagram indicate a solid phase whereas empty regions indicate dissolution of iron.

Figure 4.7 shows the voltammograms obtained for the second CV scan prior to hydrogen charging of one sample of each steel grade. As the potential was swept towards less negative values, the current response followed the anodic branch as depicted in the plot. The first peak, labelled as A1 occurs at a potential of -0.86 V. This peak was also observed in the work of Ozdirik et al. (at a potenital of -0.87 v) and was determined to be arising from thiourea related oxidation processes [45]. Peak A2 was observed at a potential of -0.7 V and is attributed to the oxidation of iron. Oxidation of iron was visible on the sample as a reddish brown layer over the exposed area. When the sweep direction was reversed, peak B2 formed in the cathodic branch at a potential of -1.04 V. Moreover, the areas of peak A2 and B2 were found to be quite similar. This peak was arising due to the reduction of iron which was oxidised during the forward scan. The current response for grade V steel was similar to that of grade T. The potential at which the peaks occurred was identical for both grades. This was expected, as the same redox processes, i.e., the oxidation of thiourea and iron occur in both materials. However, the intensity of

peaks was higher for grade V. This is attributed to difference in surface morphology between the two grades. During a CV scan, the sample surface undergoes continuous change via the formation and breakdown of oxide films on the surface. The exchange of ions across the films depends on the steric hindrance presented by the oxide film. The contribution of oxide layer is discussed further in Section 4.2.3.

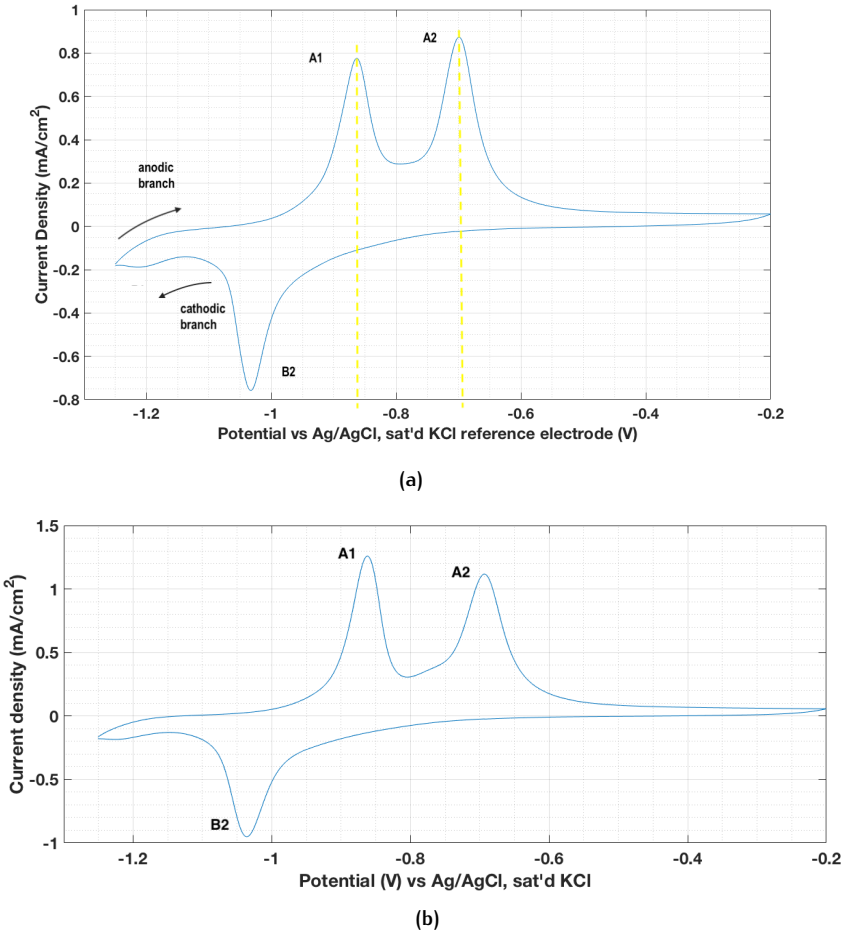

Figure 4.7: 2nd CV scan before H loading of (a) grade T steel and (b) grade V steel. Peaks A1 and A2 are due to the oxidation of thiourea and iron respectively, while peak B2 is due to the reduction of iron oxide

The CV plots for both materials post hydrogen charging are plotted in Figure 4.8. Peaks A1, A2 and B2 occurred at exactly at the same potentials as the uncharged case. However, a previously unknown peak A1' was formed at at a potential of -0.9 V for both materials. From the Pourbaix diagram, it was found that this potential corresponds to the evolution of hydrogen. During the charging step, hydrogen was evolved from the electrolyte according to Equation 2.3. The hydrogen atoms are first adsorbed or chemisorbed on the sample surface and subsurface followed by diffusion into the bulk where it may get trapped. Thus, peak A1' is attributed to diffusible hydrogen that is desorbed from the bulk of the specimen. Hydrogen that is detected via this method includes contributions from surface and subsurface sites as well as reversible traps, such as grain boundaries, in the bulk of the specimen.

Upon subsequent scanning, the hydrogen related peak disappeared, as shown in Figure 4.9. This suggested that the peak A1' was related to complete desorption of hydrogen. Peak A1 which was attributed to thiourea is also diminished significantly.

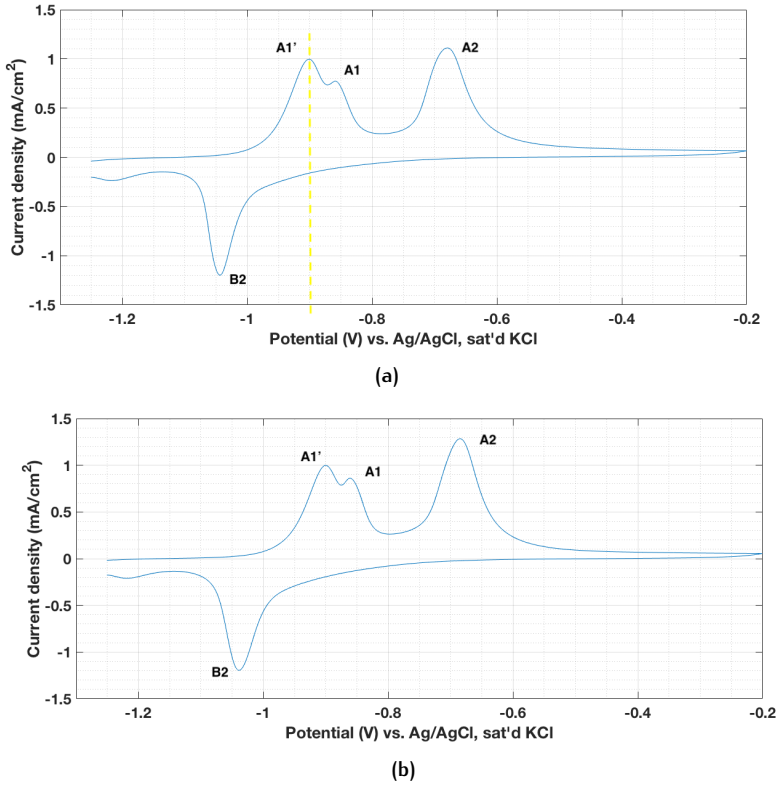

Figure 4.8: 1st CV scan post H loading of (a) grade T steel and (b) grade V steel. Apart from peaks, A1, A2 and B2, an additional peak, A1', appears at a potential of -0.9 V in both cases.

This is to be expected as some thiourea from the electrolyte is consumed to prevent hydrogen recombination, which was its intended purpose.

4.2.2 Effect of charging duration and microstructure

The hydrogen peak continued to grow with increased charging time for both materials (Figure 4.10), although the rate of increment in the peak area decreased with time. In CV, the time required for the sample to be completely saturated with hydrogen is found by repeating the charging step for increasing durations, up to the time at which the peak current from hydrogen evolution cedes to increase further. In literature, varied values for saturation time may determined by this manner may be found: four hours for as - quenched martensitic steel and two hours for DP-600 steel [45], and up to 24 hours for 304L stainless steel [46]. It must be noted that the effect of oxide layer will be more pronounced for long charging times and simultaneously, the amount of thiourea available in the electrolyte will diminish. For these reasons, the calculation of saturation time was not sought after in this work.

For quantification of the absorbed hydrogen, current transients obtained from the potentiostatic discharging step were integrated. Although discharging was done for a duration of 30 minutes, after an instantaneous rise in current, it began to drop significantly and within 100 seconds, it was almost zero (Figure 4.11). For this reason, the current-time plot was integrated up to 100 seconds. The surface charge density thus obtained was divided by the charge on an electron to obtain the number density of electrons and correspondingly that of hydrogen atoms. The number density of hydrogen atoms was then divided by the atomic density of iron to yield the concentration of hydrogen in atomic ppm. The various alloying elements were not included in this calculation as their concentration was comparatively insignificant

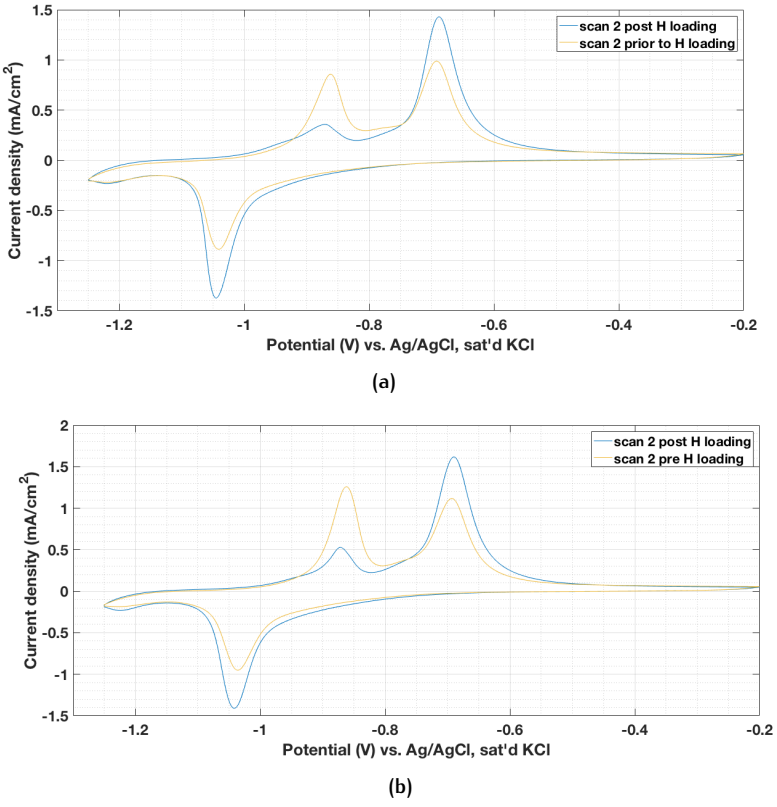

Figure 4.9: 2nd CV scan post H loading of (a) grade T steel and (b) grade V steel. The pre-charged CV plot has been added for reference. Peak A1′ no longer appears, and the shape of the plot resembles that from uncharged samples, indicating that available hydrogen was desorbed completely in this step.

to that of iron.

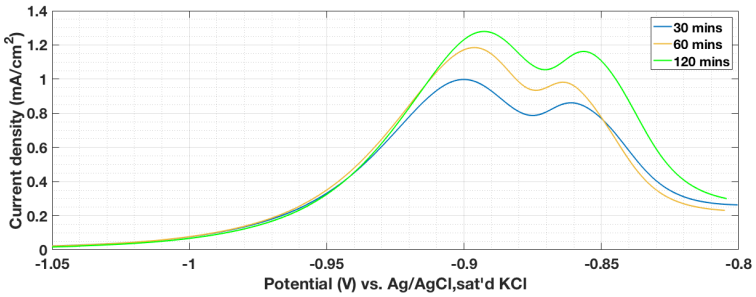

Figure 4.10: Evolution of hydrogen peaks with charging duration for grade V steel.

A comparison of hydrogen content with charging duration for the two materials is presented in Figure 4.12. The observed diffusible hydrogen content in grade V steel was consistently higher (by around 25%) than in grade T. Since the phase compositions are similar for both materials, the bulk diffusion constants for hydrogen in both materials is expected to be the same. Hence, kinetics of diffusion does not play a role in the observed difference in hydrogen concentration. It is also notable that the scatter in values obtained for grade T were consistently higher than that in grade T. Reflecting on the DFT results, off-stiochiometric vanadium carbides and nitrides were stronger traps for hydrogen which would suggest that more diffusible hydrogen should be expected in grade T steel. However, this was in contradiction with the CV results. A major source of error in CV experiments arises from the

oxide layer. The oxide was characterised to obtain more insights in this respect.

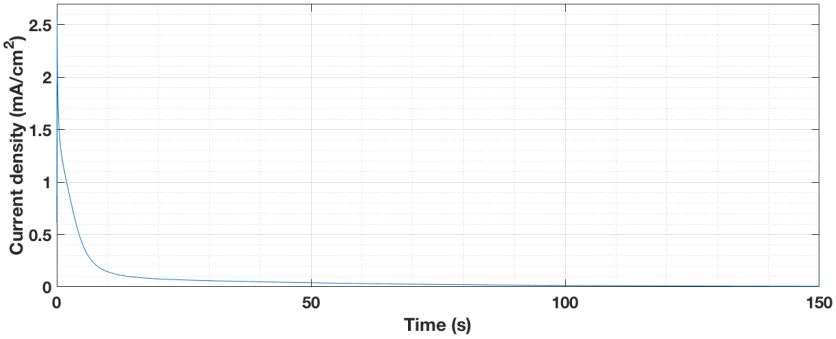

Figure 4.11: Current time transients obtained after discharging at potential of -0.9 V vs Ag/AgCl for 30 minutes for a grade V sample.

4.2.3 Contribution from oxide layer

SEM images of the oxide layer are shown in (Figure 4.13). The thickness of the oxide layer was around $2\mu m$ for both materials. However, grade V steels exhibited a uniform oxide layer throughout the activated area while that for grade T steels was sparse and irregular. This suggests that the breakdown and regeneration of oxides on grade V steel after each CV scan was, to a large extent, reversible while that was not the case for grade T. Upon contrasting the oxide film morphology against the measured hydrogen content (Figure 4.12), it is seen that the material with a larger scatter in data had a more irregular oxide morphology. As the oxide layer on grade T was more susceptible to irregularities, the number density of trap sites on the surface would also vary significantly between multiple samples, which possibly led to a large scatter in the measured hydrogen content. This observation therefore offers evidence for trapping of hydrogen by the oxide layer. Additionally, the dense layer on grade V would offer more trap sites and correspondingly more hydrogen was absorbed by this grade.

In an attempt to obtain direct evidence of hydrogen trapping by the oxide layer, FTIR spectroscopy was conducted on the V steel samples to determine whether hydrogen was bound to any of the oxide species. Figure 4.14 shows the resulting FTIR spectra. Two samples were measured: the first with two initial CV scans to generate the oxide layer (referred to as 'no charge' in the spectra) and the second with the initial CV scans followed by hydrogen charging for 120 minutes. The first group of bonds marked as O-H free are OH molecules that are not chemically bonded. OH^-

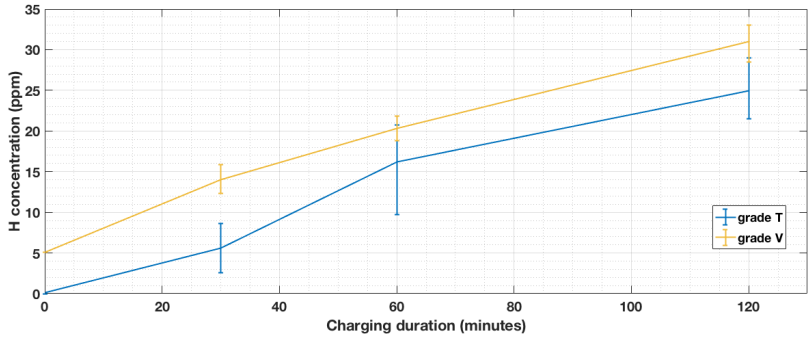

Figure 4.12: Comparison of H content in grade T and V steels

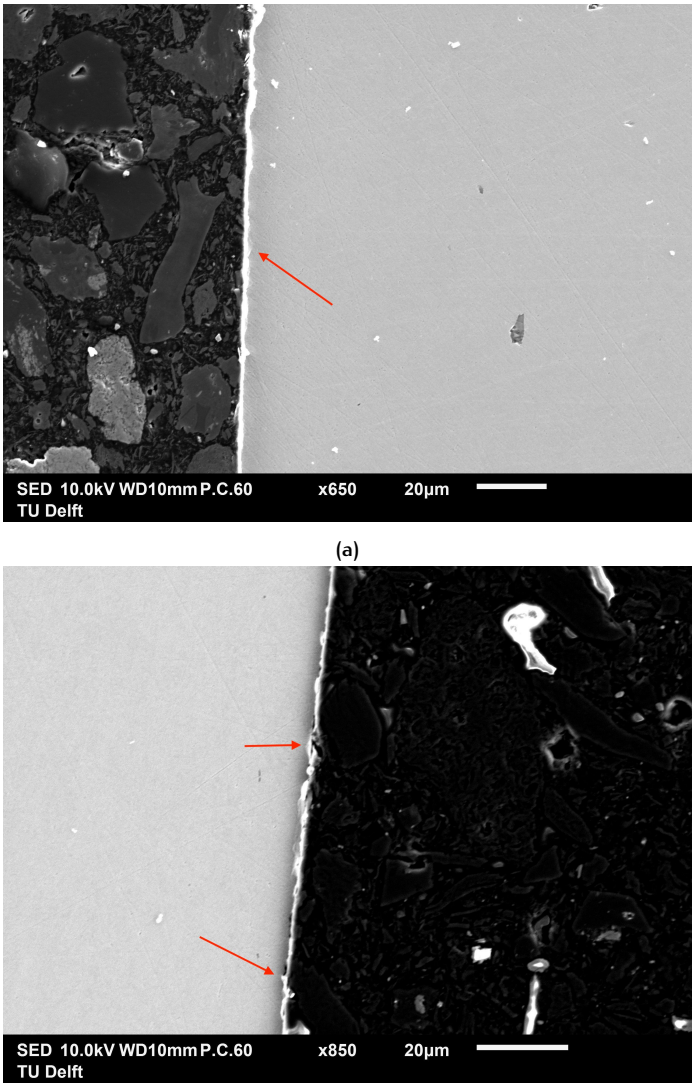

Figure 4.13: Morphology of oxide layers on (a) grade V and (b) grade T samples. While V steels had a uniform oxide layer, T steels exhibited a sparse layer.

and H^+ ions are generated on the metal surface according to the Volmer reaction (Equation 2.3). 'Free' ions on the surface can occur when larger compounds sterically hinder hydrogen bonding. The intramolecular OH bonds are expected to be coming from the (hydr)oxidation of iron. At frequencies close to 1500 cm^{-1}, a group of compounds was detected. The individual molecular species were identified as N-O, C-H and S=O. This group of molecular bonds is possibly arising from the oxidation products of thiourea, which were deposited on the metal surface. In [45], it was speculated that during CV experiments on steel in a thiourea containing solution, partial hydrogen absorption was due to the oxidation of thiourea, however any thiourea related species could not be detected with XPS and Raman spectroscopy.

Comparing the spectra of charged and uncharged samples, it is seen that the charged sample had a higher intensity of free O-H groups. This is due to hydrogen evolution in the charging step which led to the generation of more OH^- ions. Further, the intensities of species related to oxidation products of iron and thiourea decreased after charging. This could possibly be related to the breakdown of oxide layer. It has been reported that organic anions which are adsorbed at the surface may weaken the Fe-O bonds and thereby increase dissolution [55]. It was, however,

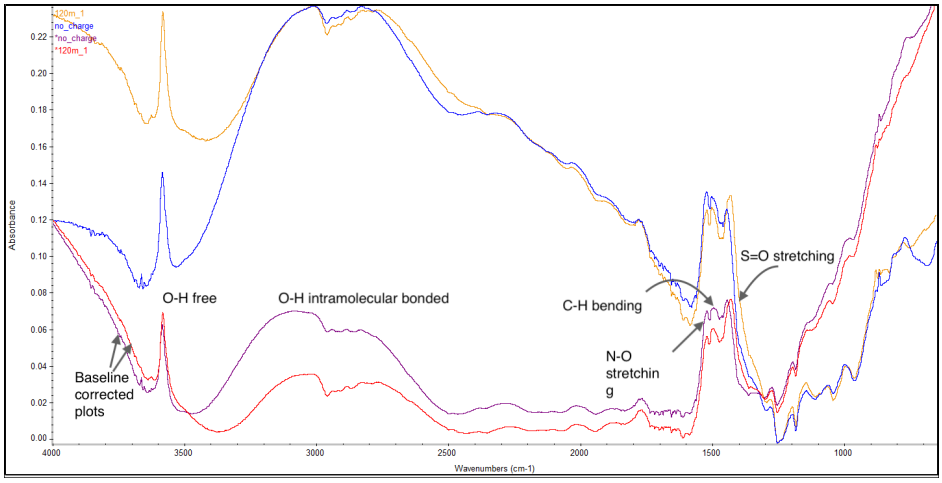

Figure 4.14: FTIR spectra of hydrogen charged and uncharged specimen

not possible to categorically identify trapped hydrogen on the oxide layer by this method.

5 CONCLUSION

This work was focused on the role of microstructure and specifically precipitates in the amount of diffusible and trapped hydrogen present in steel. The main objective of the work was to determine whether increasing the concentration of titanium or vanadium in steel would have an impact on the amount of diffusible hydrogen that may be absorbed. DFT calculations were performed to compare the hydrogen dissolution energy in carbides and nitrides of vanadium and titanium. To validate the theoretical findings, CV experiments were performed in two chemically similar grades of DP800 steel with varying concentrations of vanadium and titanium. The main conclusions from this study are listed below.

1. DFT calculations on vanadium and titanium carbides and nitrides revealed that hydrogen trapping in interstitial sites was endothermic, indicating that trapping was unfavourable. At the same time, trapping in carbon/nitrogen vacancy was exothermic. Among the carbides, a vacancy in titanium carbide was found to be the strongest trap (-0.91 eV versus -0.06 eV for vanadium carbide). However, the vacancy formation energy in titanium carbides was found to be endothermic. The vacancy - hydrogen complex formation energy, which was defined as the energy required for creation of a vacancy and subsequent trapping of hydrogen in that vacancy, was found to be more favourable in vanadium carbide than in titanium carbide (-0.89 eV to -0.22 eV). Similarly, vanadium nitride was also found to be stronger trap as compared with titanium nitride and overall, nitrides of both elements were stronger hydrogen traps. Thus, vanadium precipitates were more efficient traps for hydrogen than titanium. Correspondingly, under the same charging conditions, grade V steel would theoretically have less diffusible hydrogen, provided the number density of precipitates in both materials does not vary significantly.

2. CV results showed that the amount of diffusible hydrogen after two hours of hydrogen charging was approximately 25% higher in grade V steel than in grade T steel. This was in contradiction with the results from DFT calculations. A major error in quantitative CV experiments arises from the formation of an oxide layer on the sample surface upon CV cycling. Indirect evidence of hydrogen trapping by the oxide layer was obtained through SEM characterisation. The oxide layer on grade T steel was susceptible to irregularities, which led to a large scatter in the measured hydrogen content for this grade. Simultaneously, the oxide layer on grade V steel was uniform and dense, which provided several adsorption sites for hydrogen on the surface. During the final CV scan, the loosely bound hydrogen atoms were desorbed which led to the observed high amount of diffusible hydrogen in this grade. Direct evidence of hydrogen trapped by the oxide layer could not be obtained through FTIR spectroscopy.

6 RECOMMENDATIONS

- For using computational methods for modelling the microstructure, a good foundation is to characterise all the features that may play a role in the properties of interest. In context of the present work, precipitate stoichiometry and their number density are crucial parameters, information on which could not be obtained through HRSEM. In this regard, Transmission Electron Microscopy would be a better characterisation method, however it was not feasible in this study. Going forward, for studies involving a combination of computational and experimental methods, TEM is recommended for characterisation of microstructure.
- In the case DFT calculations on titanium carbide, it was seen that vacancy formation was unfavourable at zero temperature, but that hydrogen trapping in an already existing vacancy was quite strong. Finite temperature-DFT calculations would prove useful in resolving such issues, as the effect of temperature on vacancy formation could also be taken into account. Also, the number of hydrogen atoms that may be trapped at a single site and the subsequent change in binding energy with each hydrogen atom is another significant parameter in regard to limiting the amount of diffusible hydrogen. Further, hydrogen trapping at the precipitate-matrix interface could also be explored.
- With respect to the CV experiments, quantifying the contribution of oxide layer to hydrogen adsorption will be useful in establishing the method for quantitative analysis. Certain experimental and computational methods such as Kelvin probe method [56] or Finite Element Analysis based hydrogen transport model [57] have been proposed for this very purpose. Ab initio calculations on the trapping of hydrogen by oxides can also provide valuable insights in this regard.
- Also concerning the oxide, it was not possible to explain the discrepancy in the morphology of oxide layer on both materials. It is possible that the surface concentration of alloying elements was different in both materials. Characterisation of the oxide using chemical analysis methods such as Auger Electron Microscopy could prove to be insightful.
- Finally, the present work does not entail any mechanical testing. The next step would be to follow up with tests on edge ductility and to ascertain whether the improvements obtained by selectively precipitating strong hydrogen traps are sufficient for obtaining the desired performance level with regards to HE.

BIBLIOGRAPHY

[1] D. Fan and H. Pielet, "Bend failure mechanism of zinc coated advanced high strength steel," *ISIJ International*, vol. 58, pp. 1538–1544, 2018.

[2] "The future of hydrogen," *International Energy Agency, Paris*, 2019. [Online]. Available: https://www.iea.org/reports/the-future-of-hydrogen

[3] W. W. Gerberich, R. A. Oriani, M. Lji, X. Chen, and T. Foecke, "Necessity of both plasticity and brittleness in the fracture thresholds of iron," *Philosophical Magazine A: Physics of Condensed Matter, Structure, Defects and Mechanical Properties*, vol. 63, pp. 363–376, 1991.

[4] P. Ferreira, I. Robertson, and H. Birnbaum, "Hydrogen effects on the interaction between dislocations," *Acta Materiallia*, vol. 46, pp. 1749–1757, 1998.

[5] A. A. Pisarev, "Hydrogen adsorption on the surface of metals," in *Gaseous HE of Materials in Energy Technologies*. Woodhead Publishing Limited, 2012, ch. 1, pp. 1–26.

[6] A. Pundt and R. Kirchheim, "HYDROGEN IN METALS: Microstructural aspects," *Annual Review of Materials Research*, vol. 36, no. 1, pp. 555–608, Aug. 2006. [Online]. Available: https://doi.org/10.1146/annurev.matsci.36.090804.094451

[7] J. Takahashi, K. Kawakami, Y. Kobayashi, and T. Tarui, "The first direct observation of hydrogen trapping sites in TiC precipitation-hardening steel through atom probe tomography," *Scripta Materialia*, vol. 63, no. 3, pp. 261–264, Aug. 2010. [Online]. Available: https://doi.org/10.1016/j.scriptamat.2010.03.012

[8] B. Malard, B. Remy, C. Scott, A. Deschamps, J. Chêne, T. Dieudonné, and M. Mathon, "Hydrogen trapping by VC precipitates and structural defects in a high strength fe–mn–c steel studied by small-angle neutron scattering," *Materials Science and Engineering: A*, vol. 536, pp. 110–116, Feb. 2012. [Online]. Available: https://doi.org/10.1016/j.msea.2011.12.080

[9] A. Laureys, L. Claeys, T. D. Seranno, T. Depover, E. V. den Eeckhout, R. Petrov, and K. Verbeken, "The role of titanium and vanadium based precipitates on hydrogen induced degradation of ferritic materials," *Materials Characterization*, vol. 144, pp. 22–34, Oct. 2018. [Online]. Available: https://doi.org/10.1016/j.matchar.2018.06.030

[10] M. Aoki, H. Saito, M. Mori, Y. Ishida, and M. Nagumo, "Deformation microstructures of a low carbon steel characterized by tritium autoradiography and thermal desorption spectroscopy," *Journal of the Japan Institute of Metals*, vol. 58, no. 10, pp. 1141–1148, 1994. [Online]. Available: https://doi.org/10.2320/jinstmet1952.58.10_1141

[11] R. G. Compton, *Understanding voltammetry : problems and solutions*. London Singapore Hackensack, N.J: Imperial College Press Distributed by World Scientific Pub, 2012.

[12] O. Barrera, D. Bombac, Y. Chen, T. Daff, E. Galindo-Nava, P. Gong, D. Haley, R. Horton, I. Katzarov, J. Kermode, C. Liverani, M. Stopher, and F. Sweeney, "Understanding and mitigating hydrogen embrittlement of steels: a review of experimental, modelling and design progress from atomistic to continuum," *Journal of Materials Science*, vol. 53, pp. 6251–6290, 2018.

[13] W. H. Johnson, "On some remarkable changes produced in iron and steel by the action of hydrogen and acids." *Proceedings of the Royal Society of London*, vol. 23, pp. 168–179, 1875.

[14] T. Hilditch, T. de Souza, and P. Hodgson, "Properties and automotive applications of advanced high-strength steels (AHSS)," in *Welding and Joining of Advanced High Strength Steels (AHSS)*. Elsevier, 2015, pp. 9–28. [Online]. Available: https://doi.org/10.1016/b978-0-85709-436-0.00002-3

[15] J. A. Heikkala and A. J. Väisänen, "Usability testing of ultra high-strength steels," in *Volume 4: Advanced Manufacturing Processes Biomedical Engineering Multiscale Mechanics of Biological Tissues Sciences, Engineering and Education Multiphysics Emerging Technologies for Inspection and Reverse Engineering Advanced Materials and Tribology*. American Society of Mechanical Engineers, Jul. 2012. [Online]. Available: https://doi.org/10.1115/esda2012-82770

[16] I. Katzarov and A. Paxton, "Hydrogen embrittlement ii. analysis of hydrogen-enhanced decohesion across (111) planes in α-fe," *Physical Review Materials*, vol. 1, p. 033603, 2017.

[17] S. Wang, M. Martin, I. Robertson, and P. Sofronis, "Effect of hydrogen environment on the separation of fe grain boundaries." *Acta Materiallia*, vol. 107, pp. 279–288, 2016.

[18] C. Beachem, "A new model for hydrogen-assisted cracking (hydrogen embrittlement)," *Metallurgical and Materials Transactions*, vol. 3, pp. 441–455, 1972.

[19] O. Barrera and A. Cocks, "Computational modelling of hydrogen embrittlement in welded structures," *Philosophical Magazine*, vol. 93, no. 20, pp. 2680–2700, Jul. 2013. [Online]. Available: https://doi.org/10.1080/14786435.2013.785638

[20] T. Kanezaki, C. Narazaki, Y. Mine, S. Matsuoka, and Y. Murakami, "Effects of hydrogen on fatigue crack growth behavior of austenitic stainless steels," *International Journal of Hydrogen Energy*, vol. 33, no. 10, pp. 2604–2619, May 2008. [Online]. Available: https://doi.org/10.1016/j.ijhydene.2008.02.067

[21] M. Nagumo, "Hydrogen related failure of steels – a new aspect," *Materials Science and Technology*, vol. 20, no. 8, pp. 940–950, 2004.

[22] S. P. Lynch, "A fractographic study of hydrogen-assisted cracking and liquid-metal embrittlement in nickel," *Journal of Materials Science*, vol. 21, no. 2, pp. 692–704, Feb. 1986. [Online]. Available: https://doi.org/10.1007/bf01145543

[23] H. K. D. H. Bhadeshia, "Prevention of hydrogen embrittlement in steels," *ISIJ International*, vol. 56, no. 1, pp. 24–36, 2016. [Online]. Available: https://doi.org/10.2355/isijinternational.isijint-2015-430

[24] J. P. Hirth, "Effects of hydrogen on the properties of iron and steel," *Metallurgical Transactions A*, vol. 11, no. 6, pp. 861–890, Jun. 1980. [Online]. Available: https://doi.org/10.1007/bf02654700

[25] A. V. Uluc, *Hydrogen sorption and desorption properties of Pd-alloys and steels investigated by electrochemical methods and mass spectrometry*. TU Delft, The Netherlands, 2015.

[26] T. Depover, O. Monbaliu, E. Wallaert, and K. Verbeken, "Effect of ti, mo and cr based precipitates on the hydrogen trapping and embrittlement of Fe–C–X Q&T alloys," *International Journal of Hydrogen Energy*, vol. 40, no. 47, pp. 16 977–16 984, Dec. 2015. [Online]. Available: https://doi.org/10.1016/j.ijhydene.2015.06.157

[27] D. D. Stefano, R. Nazarov, T. Hickel, J. Neugebauer, M. Mrovec, and C. Elsässer, "First-principles investigation of hydrogen interaction with TiC precipitates in-fe," *Physical Review B*, vol. 93, no. 18, May 2016. [Online]. Available: https://doi.org/10.1103/physrevb.93.184108

[28] S. Taketomi, R. Matsumoto, and N. Miyazaki, "Atomistic study of hydrogen distribution and diffusion around a {112} 111 edge dislocation in alpha iron," *Acta Materialia*, vol. 56, no. 15, pp. 3761–3769, Sep. 2008. [Online]. Available: https://doi.org/10.1016/j.actamat.2008.04.011

[29] G. Lu and E. Kaxiras, "Hydrogen embrittlement of aluminum: The crucial role of vacancies," *Physical Review Letters*, vol. 94, no. 15, Apr. 2005. [Online]. Available: https://doi.org/10.1103/physrevlett.94.155501

[30] Y. Fukai and N. Okuma, "Evidence of copious vacancy formation in ni and pd under a high hydrogen pressure," *Japanese Journal of Applied Physics*, vol. 32, no. Part 2, No. 9A, pp. L1256–L1259, Sep. 1993. [Online]. Available: https://doi.org/10.1143/jjap.32.l1256

[31] R. Nazarov, T. Hickel, and J. Neugebauer, "Ab initiostudy of h-vacancy interactions in fcc metals: Implications for the formation of superabundant vacancies," *Physical Review B*, vol. 89, no. 14, Apr. 2014. [Online]. Available: https://doi.org/10.1103/physrevb.89.144108

[32] T. Asaoka, C. Dagbert, M. Aucouturier, and J. Galland, "Quantitative study of trapping characteristics of h in a fe-0.15% ti ferrite by high-resolution autoradiography and during degassing at high temperatures," *Scr. Metall.*, vol. 11, no. 3, pp. 467–472, 1977.

[33] T. N. Baker, "Titanium microalloyed steels," *Ironmaking & Steelmaking*, vol. 46, no. 1, pp. 1–55, Apr. 2018. [Online]. Available: https://doi.org/10.1080/03019233.2018.1446496

[34] N. Kamikawa, M. Hirohashi, Y. Sato, E. Chandiran, G. Miyamoto, and T. Furuhara, "Tensile behavior of ferrite-martensite dual phase steels with nano-precipitation of vanadium carbides," *ISIJ International*, vol. 55, no. 8, pp. 1781–1790, 2015. [Online]. Available: https://doi.org/10.2355/isijinternational.isijint-2015-106

[35] C. H. Li, C. Y. Chen, S. P. Tsai, and J. R. Yang, "Microstructure characterization and strengthening behavior of dual precipitation particles in cu ti microalloyed dual-phase steels," *Materials & Design*, vol. 166, p. 107613, Mar. 2019. [Online]. Available: https://doi.org/10.1016/j.matdes.2019.107613

[36] P. Popelier, *Solving the Schrodinger equation : has everything been tried*. London: Imperial College Press, 2011.

[37] G. Kresse and J. Hafner, "Ab initiomolecular dynamics for open-shell transition metals," *Physical Review B*, vol. 48, no. 17, pp. 13 115–13 118, Nov. 1993. [Online]. Available: https://doi.org/10.1103/physrevb.48.13115

[38] G. Kresse and J. Furthmüller, "Efficient iterative schemes forab initiototal-energy calculations using a plane-wave basis set," *Physical Review B*, vol. 54, no. 16, pp. 11 169–11 186, Oct. 1996. [Online]. Available: https://doi.org/10.1103/physrevb.54.11169

[39] J. P. Perdew, K. Burke, and M. Ernzerhof, "Generalized gradient approximation made simple," *Physical Review Letters*, vol. 77, no. 18, pp. 3865–3868, Oct. 1996. [Online]. Available: https://doi.org/10.1103/physrevlett.77.3865

[40] M. Methfessel and A. T. Paxton, "High-precision sampling for brillouin-zone integration in metals," *Physical Review B*, vol. 40, no. 6, pp. 3616–3621, Aug. 1989. [Online]. Available: https://doi.org/10.1103/physrevb.40.3616

[41] H. J. Monkhorst and J. D. Pack, "Special points for brillouin-zone integrations," *Physical Review B*, vol. 13, no. 12, pp. 5188–5192, Jun. 1976. [Online]. Available: https://doi.org/10.1103/physrevb.13.5188

[42] M. A. V. Devanathan, Z. Stachurski, and W. Beck, "A technique for the evaluation of hydrogen embrittlement characteristics of electroplating baths," *Journal of The Electrochemical Society*, vol. 110, no. 8, p. 886, 1963. [Online]. Available: https://doi.org/10.1149/1.2425894

[43] C. Dong, Z. Liu, X. Li, and Y. Cheng, "Effects of hydrogen-charging on the susceptibility of x100 pipeline steel to hydrogen-induced cracking," *International Journal of Hydrogen Energy*, vol. 34, no. 24, pp. 9879–9884, Dec. 2009. [Online]. Available: https://doi.org/10.1016/j.ijhydene.2009.09.090

[44] M. Mohtadi-Bonab, M. Eskandari, K. Rahman, R. Ouellet, and J. Szpunar, "An extensive study of hydrogen-induced cracking susceptibility in an API x60 sour service pipeline steel," *International Journal of Hydrogen Energy*, vol. 41, no. 7, pp. 4185–4197, Feb. 2016. [Online]. Available: https://doi.org/10.1016/j.ijhydene.2016.01.031

[45] B. Ozdirik, T. Depover, L. Vecchi, K. Verbeken, H. Terryn, and I. D. Graeve, "Comparison of electrochemical and thermal evaluation of hydrogen uptake in steel alloys having different microstructures," *Journal of The Electrochemical Society*, vol. 165, no. 11, pp. C787–C793, 2018. [Online]. Available: https://doi.org/10.1149/2.0891811jes

[46] K. S. E. Flores, *Study of Hydrogen Sorption/Desorption Effect on Austenitic Iron-Based Alloys*. Delft University of Technology, Netherlands, 2019.

[47] S. W. Ooi, T. I. Ramjaun, C. Hulme-Smith, R. Morana, M. Drakopoulos, and H. K. D. H. Bhadeshia, "Designing steel to resist hydrogen embrittlement part 2 – precipitate characterisation," *Materials Science and Technology*, vol. 34, no. 14, pp. 1747–1758, Jul. 2018. [Online]. Available: https://doi.org/10.1080/02670836.2018.1496536

[48] S. G. Hashemi and B. Eghbali, "Analysis of the formation conditions and characteristics of interphase and random vanadium precipitation in a low-carbon steel during isothermal heat treatment," *International Journal of Minerals, Metallurgy, and Materials*, vol. 25, no. 3, pp. 339–349, Mar. 2018. [Online]. Available: https://doi.org/10.1007/s12613-018-1577-8

[49] S. E. Restrepo, D. D. Stefano, M. Mrovec, and A. T. Paxton, "Density functional theory calculations of iron - vanadium carbide interfaces and the effect of hydrogen," *International Journal of Hydrogen Energy*, vol. 45, no. 3, pp. 2382–2389, Jan. 2020. [Online]. Available: https://doi.org/10.1016/j.ijhydene.2019.11.102

[50] R. Yang, C. Zhu, Q. Wei, and Z. Du, "Investigations on structural, elastic, thermodynamic and electronic properties of TiN, Ti2N and Ti3N2 under high pressure by first-principles," *Journal of Physics and Chemistry of Solids*, vol. 98, pp. 10–19, Nov. 2016. [Online]. Available: https://doi.org/10.1016/j.jpcs.2016.05.012

[51] H. Li, L. Zhang, Q. Zeng, K. Guan, K. Li, H. Ren, S. Liu, and L. Cheng, "Structural, elastic and electronic properties of transition metal carbides TMC (TM=ti, zr, hf and ta) from first-principles calculations," *Solid State*

Communications, vol. 151, no. 8, pp. 602–606, Apr. 2011. [Online]. Available: https://doi.org/10.1016/j.ssc.2011.02.005

[52] J. Wan, C. Wang, Q. Tang, X. Gu, and M. He, "First-principles study of vanadium carbides as electrocatalysts for hydrogen and oxygen evolution reactions," *RSC Advances*, vol. 9, no. 64, pp. 37 467–37 473, 2019. [Online]. Available: https://doi.org/10.1039/c9ra06539c

[53] F. Kubel, W. Lengauer, K. Yvon, K. Knorr, and A. Junod, "Structural phase transition at 205 k in stoichiometric vanadium nitride," *Physical Review B*, vol. 38, no. 18, pp. 12 908–12 912, Dec. 1988. [Online]. Available: https://doi.org/10.1103/physrevb.38.12908

[54] T. Epicier, D. Acevedo, and M. Perez, "Crystallographic structure of vanadium carbide precipitates in a model Fe-C-V steel," *Philosophical Magazine*, vol. 88, no. 1, pp. 31–45, Jan. 2008. [Online]. Available: https://doi.org/10.1080/14786430701753816

[55] U. SCHWERTMANN, "Solubility and dissolution of iron oxides," *Plant and Soil*, vol. 130, no. 1/2, pp. 1–25, 1991. [Online]. Available: http://www.jstor.org/stable/42937281

[56] S. Evers, C. Senöz, and M. Rohwerder, "Hydrogen detection in metals: a review and introduction of a kelvin probe approach," *Science and Technology of Advanced Materials*, vol. 14, no. 1, p. 014201, Mar. 2013. [Online]. Available: https://doi.org/10.1088/1468-6996/14/1/014201

[57] L. Vecchi, D. Pecko, N. V. den Steen, M. H. Mamme, B. Özdirik, D. V. Laethem, Y. V. Ingelgem, J. Deconinck, and H. Terryn, "A modelling approach on the impact of an oxide layer on the hydrogen permeation through iron membranes in the devanathan-stachurski cell," *Electrochimica Acta*, vol. 286, pp. 139–147, Oct. 2018. [Online]. Available: https://doi.org/10.1016/j.electacta.2018.08.022